Renewable Energy 234 (2024) 121194

Contents lists available at ScienceDirect

Renewable Energy

journal homepage: www.elsevier.com/locate/renene

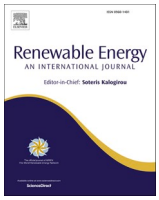

Dynamic modeling of polymer electrolyte membrane fuel cells under real-world automotive driving cycle with experimental validation on segmented single cell

Francesco Verducci, Amedeo Grimaldi *, Elena Colombo, Andrea Casalegno, Andrea Baricci

Politecnico di Milano, Department of Energy, Via Lambruschini 4, 20156, Milano, Italy

A B S T R A C T

A 1+1D transient non-isothermal and multiphase polymer electrolyte membrane fuel cell model is developed. The model is validated on experimental data gathered on a segmented single cell and representative of a real-world automotive driving cycle, derived from the stack protocol defined in the ID-FAST H2020 project. During Low-Power operation, cell voltage response is mainly controlled by platinum oxide and water dynamics: the low hydration significantly affects cathode inlet performance. Throughout High-Power operation, instead, voltage transients are ascribable to local mass-transport related phenomena: in particular, liquid water accumulation along the channel strongly decreases the efficiency of cathode outlet region. Finally, the effect of relative humidity at cathode channel inlet is investigated: an increase in the humidification of the air inlet stream from 30% to 50% leads to a better proton conductivity and, therefore, to a significant enhancement of the performance of cathode inlet regions, which also means a slight improvement in the average stack efficiency from 62.2% to 62.8%. Lowering RH of the air-inlet stream from 30% to 15%, a worsening of proton conductivity is observed, which exacerbates performance heterogeneities and leads to a reduction of the average stack efficiency from 62.2% to 61.5%, consistently with experimental results.

1. Introduction

In recent years, lot of attention has been devoted to the greenhouse effect and air pollution resulting from carbon emissions originating from fossil fuel combustion [1]. The integration of renewable energy into the transport sector has found to be unavoidable. The effective utilization of renewable energy necessitates the refinement of efficient energy conversion devices, with a particular emphasis on advancements in the hydrogen economy, specifically looking at the fuel cell technology, also confirmed by techno-economic analyses [2,3]. Relevant progress in the field of polymer electrolyte membrane fuel cell (PEMFC) in the last two decades was achieved, allowing automotive manufactures to successfully commercialize fuel cell electric vehicles (FCEVs). The interest received by PEMFC technology is due to several unique features: high efficiency and power density, low emissions, noise-free operation, fast start-up, fast response to load changes and modularity [4,5]. Nevertheless, there are still important improvements that are needed to accelerate the spread of the technology by either reducing the cost or extending the durability of components. Improvements of PEMFC materials can provide a major contribution to these targets in parallel with the development of proper operating strategies aimed at optimizing performance and mitigating degradation. Development of proper system control strategies, however, can be pursued only relying on effective modelling tools able to correctly describe the transient physical processes occurring in PEMFC stacks and components [6,7].

During the last two decades, a significant number of physics-based models were developed, which are categorized based on the modelling domain, incorporated physics and the inclusion of dynamic operation. Extensive literature exists on steady state modelling of the transport processes in PEMFCs, at various dimensions and physics. The initial numerical modelling employed a 1D scheme for simplicity and reduced computational time: they assumed single-phase isothermal conditions and simple membrane transport model, where membrane was assumed to be fully hydrated [8,9]. Moreover, this kind of models was able to capture distributions in either through-the-membrane electrode assembly (MEA) [10] or along-the-channel [11,12] directions. More recently, most of the models have evolved to 2D computational domains, capturing land/channel effects [13,14] or along the channel distributions [15–17]. Pseudo 3D [18,19] and 3D models [20,21] have also become popular but, even if they would allow to account for along-the-channel variations in property, as well as the flow-field geometry, their high computational cost makes them impractical for real-world simulations. On the other hand, the available computationally efficient models available in the literature typically oversimplify the

* Corresponding author.
E-mail address: amedeo.grimaldi@polimi.it (A. Grimaldi).

https://doi.org/10.1016/j.renene.2024.121194
Received 2 September 2023; Received in revised form 19 June 2024; Accepted 14 August 2024
Available online 14 August 2024

physics and cannot capture important phenomena, such as the two-phase flow [22]. Therefore, despite recent efforts, in literature there is still room for models that represents a good compromise between fidelity and computational cost. In this sense, as suggested by Ref. [23], a 1+1D geometry (also called quasi 2D) may represent a valuable solution for that kind of models that aspire to provide critical information for real-time fuel cell management. For this reason, in this work it was decided to adopt a 1+1D scheme. Since PEMFC dynamic response is becoming more and more important, transient phenomena were also analysed in recent models. For instance, Wang et al. [24] studied the dynamics voltage response of a PEMFC with flooded GDL when the operating conditions switches from highly humidified gases to drier gases highlighting that, thanks to a larger water diffusivity in anode gas diffusion layer (GDL), anode side shows a faster water loss with respect to cathode side []. Natarajan et al. [13] developed a two-dimensional transient model for the cathode of PEMFCs, understanding that, especially at high current density, its performance was dominated by the dynamics of liquid water. They also suggested that drier inlet gas stream, as well as higher temperatures and reduced diffusion layer thickness could help to accelerate water removal and, hence, to improve cathode performance []. Recently, Goshtasbi et al. [23] developed a PEMFC model, geared toward real-time simulation on board, able to address all the main transient phenomena, namely oxide coverage, membrane, temperature and current density dynamics.

The aim of this work is to analyse the dynamic behaviour of real-world PEMFC under driving cycle operation. This goal is achieved by the development of a 1+1D transient non isothermal and multiphase model of PEMFC stack which is calibrated on steady state measurements of polarization curves, limiting current and EIS. The model is later validated against experimental data gathered on a segmented cell hardware [25] performing a specific driving cycle protocol including Low-Power and High-Power operation under variable operating conditions.

The work is organized as follows: in *Section 2*, experimental apparatus and data are described and analysed; in *Section 3*, the governing equations and the numerical implementation of the PEMFC model are provided; model calibration and validation is reported in *Section 4*, with main investigation of the phenomena occurring inside the membrane electrode assembly (MEA) under the simulation of a real-world driving cycle protocol; additionally, the effect of air humidification on stack performance during the same driving cycle protocol is analysed.

2. Materials & methods

A segmented cell hardware with an active area of 5 cm × 5 cm was used [25]. The flow field for both anode and cathode sides consist of a triple serpentine made by three parallel channels. Both at anode and cathode side the graphite flow plates are segmented into four sections, such to separate four different portions of non-uniform active area: segment 1 = 5.83 cm^2, segment 2 = 5.80 cm^2, segment 3 = 7.65 cm^2 and segment 4 = 5.72 cm^2. The cell is operated in a counter-flow configuration and segment numbering follows the air flow, which enters in segment 1 while hydrogen stream enters in segment 4, as visible in Fig. 1 (a).

A complete set of data was used to calibrate and validate the PEMFC model, consisting in local polarization curves, whose operating conditions are listed in Table 1, limiting current density tests and driving load cycle operation. For completeness, in the Supplementary Information (SI) also Electrochemical Impedance Spectra (EIS) test is shown. Polarization curves were evaluated, considering the operating window from high to low current density values and for each current density the holding time was equal to 180 s and the average was performed on the last 120 s. In curve “oxygen”, pure oxygen is fed on the cathode side, in fully humidified conditions, whereas for curve “reference” and “dry”, air feed is used, with fully humidified conditions and with drier conditions both for anode and cathode, respectively. Limiting current tests were arranged considering three oxygen dilutions in nitrogen, specifically,

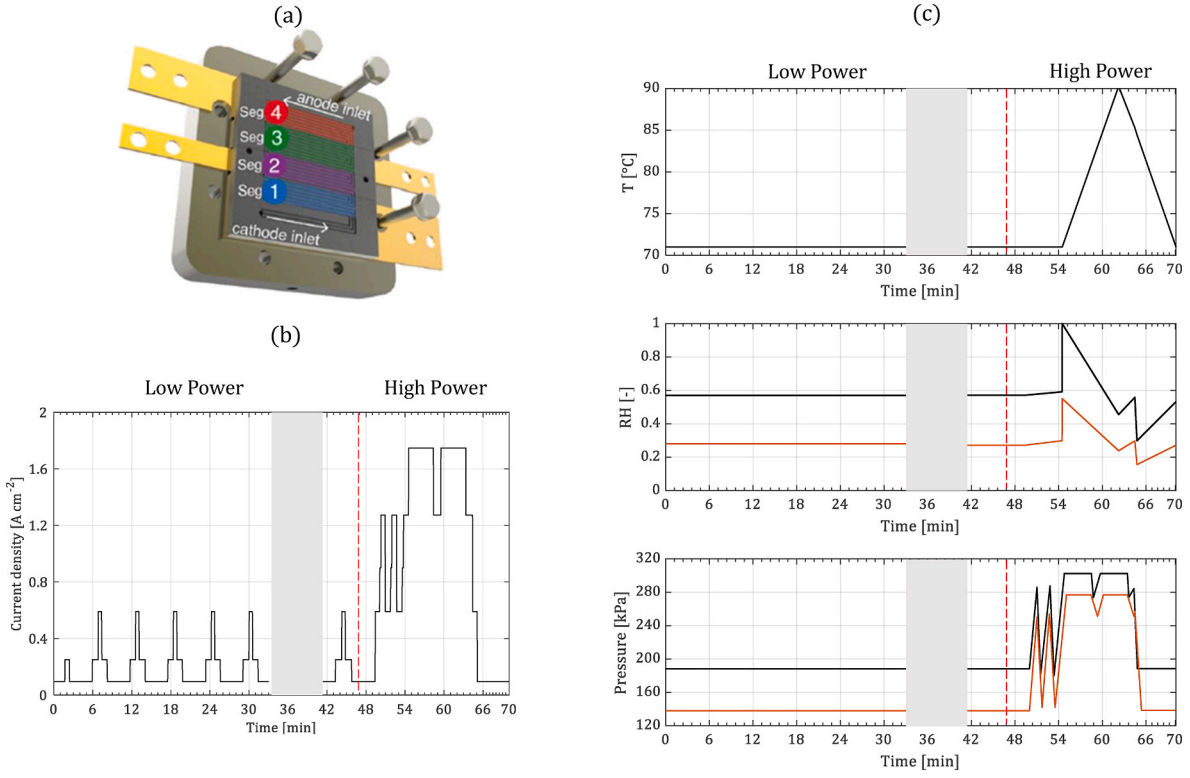

Fig. 1. – (a) Experimental hardware layout for segmented cell. Reproduced with permission from Ref. [25] (b) Load profile and (c) Operating conditions of ID-FAST driving cycle.

Table 1
Operating conditions of polarization curves.

Label	RHc	RHa	T	P_a	P_c	λ_a	λ_c	$y_{O_2,dry}$
	[−]	[−]	[°C]	[kPa]	[kPa]	[−]	[−]	[−]
Oxygen	0.999	0.999	80	250	230	2	20	0.999
Reference	0.999	0.999	80	250	230	2	4	0.209
Dry	0.3	0.5	80	250	230	2	4	0.209

1%, 2% and 3%, and three different pressure at cathode/anode inlet, p_{in} = 200 kPa, 310 kPa, 350 kPa. Cell voltage was held for 3 min at 0.4 V and then lowered to 0.3, 0.25 and 0.2 V, held 3 min per each, and the resulting average current density was recorded.

The ID-FAST drive cycle, representing the load cycle of the fuel cell system, was generated within the consortium of European ID-FAST H2020 project [26], using extensive real-world vehicle data gathered from customers, specifically detailing the relationship between vehicle speed and time. The power cycle of the fuel cell system was acquired through the application of a hybridization model for either the vehicle or powertrain, including data on the temperature variations of the fuel cell stack over time. Assessing power transitions in aggregated data and relying on proprietary fuel cell system model and experiments [27], it was possible to derive a load driving cycle, integrating stop periods with peculiar features, as reported in Ref. [25]. The obtained load driving cycle, as shown in Fig. 1(b), is composed of a Low-Power (LP) and a High-Power (HP) operating window, separated by a short-stop procedure. Low-Power region lasts approximately 60% of the whole duration and is characterized by cell voltage and current density, ranging among 0.85 and 0.7 V and 0.095 A cm^{-2} and 0.59 A cm^{-2}, respectively. The second part, instead, takes 40% of the whole driving cycle duration and, being characterized by cell voltage and current density ranging respectively among 0.85 and 0.6 V and 0.095 A cm^{-2} and 1.75 A cm^{-2}, it is representative of high engine load. To mimic real operation of fuel cell system, both cell temperature and pressures are varied accordingly to PEMFC operation, as visible in Fig. 1(c). Specifically, during Low-Power operation, temperature and reactant pressures are kept constant, respectively to 71 °C and 140 and 190 kPa for cathode and anode side. During High-Power operation, cell temperature was increased up to 90 °C through a symmetric triangular profile and reactant pressures are varying proportionally with stack load. The dew point temperatures of reactant air and hydrogen are constant during Low-Power operation, while they are changed according to Fig. 1(c) during High-Power operation. Stoichiometry is set constant to 1.4/1.6 for anode and cathode respectively.

3. Model formulation

The model developed consists in a 1+1D geometry, focusing on the through-the-membrane direction and the along-the-channel direction of the PEMFC. Therefore, for simplicity and clarity, first the 1D through-the-membrane model is introduced in Section 3.1 and the governing equations, properties and boundary conditions implemented in it are discussed. Then, in Section 3.2, the 1D along-the-channel model is described. Finally, more details concerning numerical implementation are given in Section 3.3. The following assumptions are made:

- Gaseous species are assumed to be ideal gases.
- Diffusion media and catalyst layers are isotropic and homogeneous.
- Pressure gradient in the through-MEA direction is neglected for gaseous species.
- Tafel kinetics is adopted for oxygen reduction reaction (ORR), while Butler-Volmer kinetics is adopted for hydrogen oxidation reaction (HOR).
- Double layer effects at cathode side are considered only for the simulation of the EIS spectra.
- Water is present in three phases. Evaporation/condensation mechanisms describe the phase change between liquid and vapor while absorption/desorption mechanisms govern the transition from dissolved to vapor and vice versa.
- Only crossover of hydrogen across the membrane is considered. Crossover of other species is neglected since it does not affect significantly PEMFC performance.
- Control volume (CV) approach is used to implement each transport equation, described in Section 3.1.1.
- Gas flow in the channels is assumed to be laminar due to small Reynolds number.
- Liquid water transport through porous media is considered for both anode and cathode side, whereas liquid water transport in channel is assumed to affect only species transport in cathode gas channel.
- Flow pattern of liquid water in gas channel is assumed to be comparable to a liquid film flow.
- Thermal conduction is considered for heat transfer in the porous medium
- Counter-flow configuration is implemented.

3.1. Through-MEA transport model

3.1.1. Numerical method for control-volume integration

Before introducing the specific governing equations of PEMFC for the through-MEA direction, the method of the control-volume integration used in this work is explained. In Eq. (1), the conservation equation is reported in a general form:

$$\frac{\partial \xi}{\partial t} = -\nabla \cdot \dot{n}_\xi + s_\xi \tag{1}$$

This equation is later applied for species conservation, charge conservation, liquid and adsorbed water conservation, energy conservation. In Eq. (1), ξ indicates the potential (molar concentration, electrostatic potential, liquid saturation, water content, temperature respectively). In the same equation, $\dot{n}_\xi$ is the flux and s_ξ the volumetric source associated to each variable ξ. Further details on each equation are reported later in this Section. Considering a specific sub-domain and dividing it into discrete control volumes of thickness d_{CV}, the nodal points are set in the centre of each control volume and the boundaries are placed mid-way between adjacent nodes, such that each control volume surrounds a node, as visible in Fig. 2. The left/right boundaries of the CV are referred as left "l" and right "r". The values of the variable ξ are evaluated at the CV centre. By integrating inside the CV the generic Eq. (1), it yields to

$$\frac{d\xi^j}{dt}\, d^j_{CV} = \dot{n}^{l,j}_\xi - \dot{n}^{r,j}_\xi + S_\xi \tag{2}$$

where $\dot{n}^{l,j}_\xi$ and $\dot{n}^{r,j}_\xi$ are the fluxes at left/right boundaries of the CV, S_ξ the source resulting from the integration of s_ξ inside the CV along the x-direction.

The flux $\dot{n}_\xi$ is driven by the gradient of the same quantity ξ and adequate transport resistances can be defined such that:

$$\dot{n}^{l,j}_\xi = \frac{\xi^{j-1} - \xi^j}{R^{j-1}_\xi + R^j_\xi} \quad \dot{n}^{r,j}_\xi = \frac{\xi^j - \xi^{j+1}}{R^j_\xi + R^{j+1}_\xi} \tag{3}$$

Two exceptions are the electroosmotic drag flux and the capillary

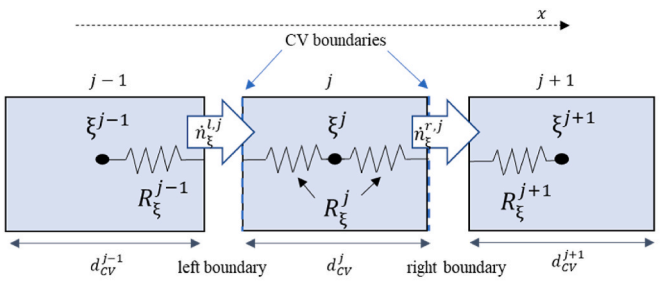

$$\frac{\partial \xi}{\partial t} = -\nabla \cdot \dot{n}_\xi + s_\xi \quad \xrightarrow{\text{CV integration in 1D along x-direction}} \quad \frac{d\xi^j}{dt} d_{CV}^j = \dot{n}_\xi^{l,j} - \dot{n}_\xi^{r,j} + S_\xi$$

Fig. 2. (a) Schematics of the numerical approach adopted to solve the conservation equation for the general variable ξ, evaluating the fluxes at the left/right boundaries of the j control volume associated to the specified variable, $\dot{n}_\xi^l$ and $\dot{n}_\xi^r$ respectively.

driven transport which are described in Sections 3.1.4 and 3.1.3 respectively. Boundary conditions are applied to the extreme CVs at the respective CV boundary, depending on the specific boundary-condition typology, i.e. imposed value of the variable ξ and/or imposed flux $\dot{n}_\xi$.

3.1.2. Transport of gaseous species through porous layers

Along the through-MEA direction seven subdomains are considered: GDLs, MPLs, CLs both for anode and cathode sides, together with the proton-exchange membrane (PEM). Each of those subdomains is divided into a certain number of control volumes (CVs), as shown in Section 3.3.

Gas species transport all over porous media is described by Eq. (4) for each CV:

$$\frac{d}{dt}\left(\varepsilon_{gas} c_i^j\right) d_{CV} = \frac{c_i^{j-1} - c_i^j}{R_{gas}^{j-1} + R_{gas}^j} - \frac{c_i^j - c_i^{j+1}}{R_{gas}^j + R_{gas}^{j+1}} + S_i \tag{4}$$

where ε_{gas} is the porosity of the layer, occupied by gas, $\varepsilon_{gas} = \varepsilon(1-s)$ with s being the liquid saturation and ε the compressed layer porosity. The term on the left-hand side of Eq. (4) describes the accumulation of gas inside porous volume of the CV, while the first two terms on the right-hand side denote the diffusive fluxes coming into and exiting from the CV. S_i represents the source term for the specific gas species, which accounts for the production or consumption of species due to the electrochemical reactions or mass exchange between phases.

The rates of hydrogen and oxygen consumption are linked to the electrochemical reaction rates and they are taken into account only in the anodic and cathodic catalyst layers: $S_{H_2} = -\frac{1}{2F}\left(i_{HOR} + i_{H_2,crossover}\right)$ and $S_{O_2} = -\frac{1}{4F} i_{ORR}$, where the term $i_{H_2,crossover}$ accounts for hydrogen crossover across membrane (Section 3.1.2). Concerning the phase change term, S_{vl}, which interests only water vapor, further details will be provided in the following lines. More information about the expression of the different source terms can be found in Table 7. Gas resistances in Eq. (4) are computed by considering the effective diffusion coefficient, D_i^{eff}, of species i, as described in Table 2.

In the GDL domain, gas transport is ascribable to the molecular diffusion; the presence of the land structure is making the diffusion process in the porous region, right under the flow field structure, a two-dimensional phenomenon, increasing the diffusion path of the species. The thickness of the GDL was increased effectively to capture the increased transport length, as done in Refs. [23,31], correcting it by an additional factor f_{land}. For the MPL, it was assumed that gas diffusion is not influenced by the land structure and it remains a one-dimensional problem. Knudsen diffusion mechanism contributes to the whole diffusion process. Gas diffusion in cathode CL is discussed in Section 3.1.4.

The model includes the crossover of hydrogen across membrane, whereas crossover of oxygen and nitrogen was neglected because of their low permeabilities values [32]. For sake of clarity, gas transport is not solved inside membrane, but the resulting flux of hydrogen determined by partial pressure gradient across membrane is evaluated according to Eq. (5), assuming that no hydrogen is present at cathode side, and its consumption is considered in the mass conservation for hydrogen in CLa, as indicated in the related S_{H_2} mentioned above.

Table 2
Properties of mass transport in porous media.

Property	[Units]	Equation	Reference
R_{gas}	$[s\,m^{-1}]$	$\frac{d_{CV}}{2D_i^{eff}}$	–
D_i^{Kn}	$[m^2 s^{-1}]$	$\frac{2}{3} r_{KN} \sqrt{\frac{8}{\pi}\frac{RT}{M_i}}$	[28]
D_i^{mix}	$[m^2 s^{-1}]$	$\frac{1-y_i}{\sum_{j\neq i}^{Nspecies} \frac{y_j}{D_{i,j}}}$	[29]
D_i	$[m^2 s^{-1}]$	$\left(\frac{1}{D_i^{Kn}} + \frac{1}{D_i^{mix}}\right)^{-1}$	[28]
D_i^{eff}	$[m^2 s^{-1}]$	$\frac{\varepsilon}{\tau}(1-s)^{\gamma_s} D_i$	[28]
R_{liq}	$[m^{-1}]$	$\frac{d_{CV}}{2\,K_{abs}\,k_{rel}}$	–
k_{rel}	[–]	s^3	[30]

$$\dot{n}_{H_2,\mathrm{MEM}} = K_{H_2} \frac{p_{H_2}^{CLa}}{d_{MEM}} \tag{5}$$

where $p_{H_2}^{CLa}$ is the partial pressure of hydrogen in the anode CL and K_{H_2} indicates the permeability of membrane to hydrogen, reported in Table 3. Moreover, to the hydrogen crossover, a current $i_{H_2,crossover}$ is associated and it must be considered in the charge balance at cathode side, assuming that it reacts immediately with oxygen, producing water, thus it is computed according to:

$$i_{H_2,crossover} = 2\,F\,\dot{n}_{H_2,\mathrm{MEM}} \tag{6}$$

3.1.3. Liquid water transport

Liquid water is present inside porous media and gas flow channels. In porous media, liquid saturation, s, is defined as the ratio between the liquid water volume and the pore region volume. The mass conservation equation, that accounts for liquid saturation distribution across porous media, is given by Eq. (7):

$$\frac{d}{dt}\left(\varepsilon \frac{\rho_{liq}}{M_{H_2O}} s^j\right) d_{CV} = \frac{\rho_{liq}}{M_{H_2O}\,\mu_{liq}} \left(\frac{p_{cap}^{j-1} - p_{cap}^j}{R_{liq}^{j-1} + R_{liq}^j} - \frac{p_{cap}^j - p_{cap}^{j+1}}{R_{liq}^j + R_{liq}^{j+1}}\right) + S_{vl} \tag{7}$$

Table 3
Membrane water uptake and transport properties.

Property	[Units]	Equation	Reference
$\eta_{d,eff}^{l,j}$	[−]	$\frac{2.5}{22}\cdot\left(\frac{\lambda^j+\lambda^{j-1}}{2}\right)\exp\left(\frac{4000}{\mathscr{R}}\cdot\left(\frac{1}{303.15}-\frac{1}{T}\right)\right)$	[41,42,47]
$\eta_{d,eff}^{r,j}$	[−]	$\frac{2.5}{22}\cdot\left(\frac{\lambda^j+\lambda^{j+1}}{2}\right)\exp\left(\frac{4000}{\mathscr{R}}\cdot\left(\frac{1}{303.15}-\frac{1}{T}\right)\right)$	[41,42,47]
D_λ	$[m^2 s^{-1}]$	$\left(1+\frac{1.8\times10^{-5}}{EW/\rho_{ion}}\lambda\right)^{-2}\cdot0.054\cdot(1.0+2.7\times10^{-3}\lambda^2)\left[1+\tanh\left(\frac{\lambda-2.62}{0.88}\right)\right]\exp\left(-\frac{27800}{\mathscr{R}T}\right)\times10^{-4}$	[39,40]
R_λ	$[s\ m^{-1}]$	$\frac{d_{CV}}{2D_\lambda^{eff}}$	
K_{H_2}	$[mol\ m^{-1}\ s^{-1} Pa^{-1}]$	$\left(15.7\cdot\exp\left(-\frac{20280}{\mathscr{R}T}\right)+45\cdot f_v\cdot\exp\left(-\frac{18930}{\mathscr{R}T}\right)\right)\times10^{-12}$	[32]
k_{vd}	$[m\ s^{-1}]$	$6.8\times10^{-6}\cdot\lambda^{1.6}\cdot\exp\left(\frac{20000}{\mathscr{R}}\left(\frac{1}{303.15}-\frac{1}{T}\right)\right)$	[46]
λ_{eq}	[−]	$(1-\tanh(10\cdot s))\cdot\left(0.3+7\cdot RH\cdot(1-\tanh(RH-0.5))+0.69\cdot(12.2-3.52)\cdot\sqrt{RH}\cdot\left(1+\tanh\left(\frac{RH-0.92}{0.23}\right)\right)\right)+\tanh(10\cdot s)\cdot(12.2+0.181\cdot(T-273.15))$	[23,45]
f_v	[−]	$\frac{1.8\times10^{-5}\lambda}{\frac{EW}{\rho_{ion}}+1.8\times10^{-5}\lambda}$	

Table 4
Effect of temperature, relative humidity and electrode potential on local oxygen resistance.

Function	Expression	Reference
$f_1(RH)$	$\exp(-1.1\cdot(RH-1))$ if RH < 1 1 if RH ≥ 1	Fitted from experimental data in [53]
$f_2(T)$	$\exp\left(\frac{17200}{\mathscr{R}}\cdot\left(\frac{1}{T}-\frac{1}{353.15}\right)\right)$	[53]
$f_3(\Delta\varphi_c)$	$2+\tanh(6\ (\Delta\varphi_c-0.5))$	[54]

In Eq. (7), gas-phase pressure is assumed constant across porous media in the through-plane direction and liquid pressure gradient is equal to capillary pressure, p_{cap}. The dependence of water saturation on capillary pressure is described by the empirical correlation, developed by Ref. [33].

$$p_{cap}(s) = -\gamma_{liq}\cos(\vartheta_c)\sqrt{\frac{\varepsilon}{K_{abs}}}\left(1.417\,s-2.120\,s^2+1.263\,s^3\right) \tag{8}$$

where K_{abs}, representing the absolute permeability of the porous layer, is a material property as indicated in Table A1 of the Appendix. The Leverett J-function appears to be less compliant with the fuel cell porous layers, where the water discharge capacity of the GDL is affecting local electrochemical performance [34–36]. Contact angles in GDLs and MPLs are in accordance with literature [37]. During last years, models for the liquid water transport in graphite-based porous-layer were developed, for example the mixed wettability model. Meanwhile, in the literature, experimental water retention curves are shown for some commercial gas diffusion layers, but more uncertainty is related to the catalyst layer one, because water imbibition and withdrawal into catalyst layer is very difficult to achieve [38]. Hence, no reliable measurements in literature are present for CL. It was preferred to adopt homogenously the J-Leverett approach for all the porous layers, well established in the literature. The source term S_{vl} in liquid water conservation equation (Eq. (7)) is given by the evaporation/condensation mechanism, regulating mass transfer between liquid and water vapor phases [28], and it represents the source term of the water vapor transport equation (Eq. (4)) solved in each CV in which anodic and cathodic porous layers are discretized. Further details about the source terms in the different domains of the model can be found in Table 7.

$$S_{vl} = \begin{cases} d_{CV}\,k_{vl}\,(p_v-p_{sat})s, p_v < p_{sat} \\ d_{CV}\,k_{vl}\,(p_v-p_{sat})(1-s),\ p_v \geq p_{sat} \end{cases} \tag{9}$$

3.1.4. Water uptake and transport through ionomer

The hydration of membrane and ionomer in the catalyst layers is modelled with the use of water content or hydration λ:

$$\frac{d}{dt}\left(\varepsilon_{ion}\frac{\rho_{ion}}{EW}\lambda^j\right)d_{CV} = \left(\frac{\rho_{ion}}{EW}\frac{\lambda^{j-1}-\lambda^j}{R_\lambda^{j-1}+R_\lambda^j}-\eta_{d,eff}^{l,j}\frac{i}{F}\right)-\left(\frac{\rho_{ion}}{EW}\frac{\lambda^j-\lambda^{j+1}}{R_\lambda^j+R_\lambda^{j+1}}-\eta_{d,eff}^{r,j}\frac{i}{F}\right)+S_d \tag{10}$$

For the transport of water dissolved inside the ionomer, the water diffusion and the electro-osmotic drag fluxes are included. The dissolved water diffusivity D_λ, which depends on the water content and temperature, is based on the correlation in Refs. [39,40]. The terms $\eta_{d,eff}^{l,j}\frac{i}{F}$ and $\eta_{d,eff}^{r,j}\frac{i}{F}$ in Eq. (10) represent the electro-osmotic drag fluxes, associated to the transport mechanism of water molecules, that occurs because of the drag effect caused by the flux of protons in the same ionomer domain, thus to the current density, *i*. In order to approximate the drag flux at the CV boundaries of the domain, the drag coefficient of each CV is evaluated according to Ref. [41], based on the dependence by Ref. [42], corrected with the Arrhenius equation, as in Ref. [43], and the algebraic mean is applied between adjacent CVs, as listed in Table 3. Since current density is not homogeneous in the CL, a corrective factor was introduced, similarly to the proton transport resistance in CLs, i.e. $\frac{1}{3+\zeta}$, based on correction from Ref. [44] (further details are reported in Section 3.1.6). Both the diffusivity of dissolved water D_λ and the electro-osmotic drag coefficient η_d, estimated in the CLs, are corrected for the Bruggeman correction, $\varepsilon_{ion}^{1.5}$.

The source term S_d in Eq. (11), non-null in CLs, accounts for both phase transfer with water vapor (adsorption/desorption) and water production from ORR. The former is evaluated by using the non-equilibrium membrane water sorption model proposed by Ref. [20], according to which adsorbed water inside ionomer is proportional to the difference between the local water content λ and its value at equilibrium, λ_{eq}. The water content at equilibrium, λ_{eq}, has been derived from real data taken on Nafion membranes [45]. As it is shown in Table 3, λ_{eq} accounts also for the effect of liquid water, as done by Ref. [23] and commented in the SI.

$$S_d = \begin{cases} S_{vd}+\frac{i_{ORR}}{2F}\ for\ cathode\ CL \\ S_{vd}\ for\ anode\ CL \end{cases} \tag{11}$$

$$S_{vd} = k_{vd}\,\frac{\rho_{ion}}{EW}\,(\lambda_{eq} - \lambda) \tag{12}$$

The interfacial water transport at ionomer/gas boundary can be modelled by the interfacial mass transport coefficient, k_{vd}, which depends on temperature and water content [46]. Please, refer to Table 7 for a comprehensive description of the source terms.

3.1.5. Local oxygen-transport resistance through thin-ionomer-film

Numerous works are devoted to analysing and modelling of local oxygen-transport through the ionomer thin-film covering platinum nanoparticles, particularly evident in low platinum loading CLs [48] and after ageing [49]. As shown by Refs. [23,50], assuming that Pt nanoparticles are deposited on carbon support homogeneously and are covered by both an ionomer and water films, local oxygen-transport resistance in CL is composed of several contributions (oxygen dissolution and diffusion in water, dissolution and diffusion into ionomer film). However, the lack of microstructural measurements and the CL morphological heterogeneity make harder to identify the above-mentioned contributions. Thus, the model proposed by Refs. [51,52], lumping all the contributions into one single resistance, except for the one related to oxygen dissolution into the ionomer, is adopted. The resistance, $R^{Pt}_{O_2}$, is dependent upon local operating conditions, as well as the roughness factor, that is the product of the electrochemical active surface area, *ECSA,* and the platinum loading, $L_{Pt,c}$. The oxygen flux, within the ionomer layer, can be expressed as in Ref. [52]:

$$\dot{n}^{film}_{O_2} = \frac{c^{eq}_{O_2} - c^{Pt}_{O_2}}{\frac{R^{Pt}_{O_2}}{r.f.}} \tag{13}$$

with $c^{Pt}_{O_2}$ and $c^{eq}_{O_2}$ as the local oxygen-concentration at the Pt surface and the equilibrium-concentration at the ionomer-gas interface respectively. The latter is related to the gas-phase oxygen-concentration, $c^{CL,gas}_{O_2}$, through the Henry's law [52]:

$$c^{eq}_{O_2} = \mathscr{R}\cdot T\cdot H^{cc}\cdot c^{CL,gas}_{O_2} \tag{14}$$

where $H^{cc} = 3.16 \times 10^{-5}$ mol m^{-3} Pa^{-1} is the Henry's constant of dissolved oxygen in Nafion [51]. The oxygen flux (Eq. (13)) is equal to the ORR oxygen flux, dependent upon $c^{Pt}_{O_2}$, under steady state conditions. The steady-state transport of oxygen through ionomer film is assumed in dynamic modelling [53,54] and no accumulation is included in the ionomer layer, because of its small volume [55]. Further dependence of the $R^{Pt}_{O_2}$ from the local operating conditions is included:

$$R^{Pt}_{O_2} = R^{Pt}_{O_2,ref}\cdot\frac{353.15}{T}\cdot f_1(RH)\cdot f_2(T)\cdot f_3(\Delta\varphi_c) \tag{15}$$

The factor $f_3(\Delta\varphi_c)$, as shown in Table 4, was introduced in Eq. (15) (Ref. [54]) from the evidence that in the intermediate-potential region (between 0.45 and 0.7 V vs RHE) the local oxygen-transport resistance presents an increasing trend, associated to adsorption of some species on Pt surface, especially sulfonates from the ionomer layer, which determines a decrease of the effective active area and a significant growth of the associated mass transport resistance. At low electrode potentials, the factor f_3 tends to 1, because adsorption of sulfonates is not favoured. The term $R^{Pt}_{O_2,ref}$ in Eq. (15) is linked to the total film-resistance for oxygen transport, $R^{*Pt}_{O_2,ref}$, estimated from the experimental slope of the non-Fickian component of the oxygen-transport resistance with respect to the roughness factor, *r. f.* [56].

$$R^{*Pt}_{O_2,ref} = \frac{R^{Pt}_{O_2,ref}}{H^{cc}\cdot\mathscr{R}\cdot T} \tag{16}$$

$R^{Pt}_{O_2,ref}$ is set to 111 s m^{-1} so that $R^{*Pt}_{O_2,ref}$ is equal to 1200 s m^{-1} at 80 °C, consistently with typical values reported in literature (1100–1300 s m^{-1} [57]).

3.1.6. Reaction kinetics and charge conservation

The ORR kinetics model adopted is based on the modified Tafel expression [49], accounting for the effect of ORR inhibition due to platinum oxides (PtO) through the platinum oxide coverage, ϑ_{PtO}. The oxide coverage effect was also incorporated into the ORR kinetic expression through a Temkin isotherm approach, able to consider the respective interactions between the oxide species on the Pt-sites.

$$i_{ORR} = 4\,\mathrm{F}\,K_{r,ORR}ECSA_c\,L_{Pt,c}\left(\frac{c^{Pt}_{O_2}}{c_{O_2,ref}}\right)^{0.8}(1-\vartheta_{PtO})\exp\left(-\frac{\omega_{PtO}\,\vartheta_{PtO}}{\mathscr{R}T}\right)\exp\left(-\frac{\alpha_{r,ORR}F\Delta\varphi_c}{\mathscr{R}T}\right) \tag{17}$$

where $\Delta\varphi_c$ is the applied electrode potential at cathode CL, corresponding to the difference between the electrical, φ_{el}, and the protonic potential, φ_{ion}, also equal to the sum of the equilibrium electrode potential, $E_{0,ORR}$, and the overpotential for the ORR, whereas ω_{PtO} stands for the energy parameter in the Temkin isotherm approach, quantifying the rate at which the apparent Gibb's adsorption energy of adsorbed species on the catalytic sites change with the Pt coverage. The reference oxygen concentration, $c_{O_2,ref}$, in Eq. (17) is computed as $\frac{p_{ref}}{\mathscr{R}T}$, where p_{ref} is equal to 101325 Pa and T is the local temperature in cathode CL.

The formation/reduction of PtO, highly impacting upon the dynamic cell performance and durability [58,59], is modelled, according to Ref. [49].

$$\frac{d\vartheta_{PtO}}{dt} = (1-\vartheta_{PtO})\frac{K_{o,PtO}}{\Gamma}\cdot\exp\left(\frac{\alpha_{o,PtO}\,F\Delta\varphi_c}{\mathscr{R}T}\right) - \vartheta_{PtO}\frac{K_{r,PtO}}{\Gamma}\cdot\exp\left(-\frac{\alpha_{r,PtO}\,F\Delta\varphi_c}{\mathscr{R}T}\right) \tag{18}$$

where Γ represents the adsorbed charge per unit area of platinum surface, $K_{o,PtO}$ and $K_{r,PtO}$ are the forward and backward reaction rates respectively.

Moreover, a current density linked to PtO oxidation/reduction, i_{PtO}, is established and it must be included in the charge balance in the cathode CL.

$$i_{PtO} = 2F\,ECSA_c\,L_{Pt,c}\Gamma\frac{d\vartheta_{PtO}}{dt} \tag{19}$$

HOR owns knowingly a simple and fast kinetics, with low overpotential losses under most of typical operating conditions. Therefore, here a simple Butler-Volmer kinetics model is used for its description in its general form as function of the applied electrode potential at anode CL, $\Delta\varphi_a$, corresponding to the sum of the equilibrium electrode potential and the overpotential for the HOR, and the current density is found to be:

$$i_{HOR} = 2F\,ECSA_a\,L_{Pt,a}\left(K_{o,HOR}\left(\frac{C_{H_2}}{C_{H_2,ref}}\right)^{0.5}\exp\left(\frac{\alpha_{o,HOR}F\Delta\varphi_a}{\mathscr{R}T}\right) - K_{r,HOR}\exp\left(-\frac{\alpha_{r,HOR}F\Delta\varphi_a}{\mathscr{R}T}\right)\right) \tag{20}$$

where the reference hydrogen concentration, $c_{H_2,ref}$, is calculated as described above for $c_{O_2,ref}$. Both at cathode and anode catalyst layers, charge conservation must be guaranteed, taking into account that, as already explained in Section 3.1.2, in the cathode CL an additional contribution, associated with the hydrogen crossover, $i_{H_2,crossover}$, arises:

$$i = i_{ORR} - i_{H_2,crossover} - i_{PtO} \tag{21}$$

$$i = i_{HOR} \tag{22}$$

Thus, cell voltage, common boundary condition among the different MEA segments, is:

$$\Delta V = \Delta\varphi_c - \Delta\varphi_a - \left(R_{MEM} + R_{CL}^{eff} + R_{el}\right) i \tag{23}$$

where R_{el} is constant and equals the electric resistance of GDLs and BPs, together with all the contact resistances, R_{CL}^{eff} represents the effective proton-transport resistance opposed by catalyst layer, and R_{MEM} is the proton-transport resistance opposed by the membrane, both dependent upon σ_{ion}, that is knowingly function of both water volume fraction in ionomer, f_v, and temperature, T (Table 5). Moreover, since the HOR is kinetically favoured and gas-diffusion resistances through anode CL are negligible, HOR reaction is occurring in proximity of CL/membrane interface, determining a short path for proton transport and consequently negligible ohmic losses in anode CL, assumed to be null [44]. Ion transport in cathode CL is modelled with a lumped approach, where R_{CL}^{eff} is accounting for the effective catalyst layer utilization. The approach proposed by Ref. [23] is adopted, where coefficient ς represents the polynomial fit of the solution obtained by Ref. [44].

$$R_{CL}^{eff} = \frac{d_{CL}}{\epsilon_{ion}^{1.5}\sigma_{ion}} \frac{1}{3+\varsigma} \tag{24}$$

$$\varsigma = -2.072 \times 10^{-3} + 7.184 \times 10^{-1}\,\theta - 8.287 \times 10^{-3}\,\theta^2 \tag{25}$$

being $\theta = \frac{d_{CL}}{\epsilon_{ion}^{1.5}\sigma_{ion,CL}} \frac{i}{b}$ with $b = \frac{2.303\ \alpha_{r,ORR} F}{\mathscr{R} T}$.

The experimental high-frequency resistance (HFR) is given by the two different contributions, R_{MEM}, and R_{el}, as reported in Table 5.

3.1.7. Heat transport

Temperature distribution across all the media in the through-plane direction is computed, assuming local thermal equilibrium between phases and negligible convective heat transport, as done in literature in porous structure, where Peclet number are typically low [60].

$$\frac{d}{dt}\left(C_{th} T^j\right) d_{CV} = \frac{T^{j-1} - T^j}{R_{th}^{j-1} + R_{th}^j} - \frac{T^j - T^{j+1}}{R_{th}^j + R_{th}^{j+1}} + S_{th} \tag{26}$$

with C_{th} and k_{th} are the thermal capacity and the thermal conductivity of the subdomain respectively, reported in Table 6. The source term S_{th} depends on the sub-domain region (Table 7), where $\Delta\widetilde{H}_{vl}$ and $\Delta\widetilde{H}_{ORR}$ are the specific enthalpies related to the phase change and to the ORR, respectively. The Joule effect linked to the electronic charge transport, $R_{el}\, i^2$, is subdivided into the GDLs and MPLs, proportionally to their thicknesses, through a weight factor, f_{th}.

3.1.8. 1D through-the-membrane model: boundary conditions

Boundary conditions need to be set at each interface between domains and they are listed in Table 8. The boundary condition at GDL/channel interface for liquid transport is in analogy with that implemented in the work of Pant et al. [19], properly modified to avoid numerical instabilities. Water flux is assumed to exit from GDL and enters the channel volume and no flux is entering into GDL.

$$\dot{n}_{liq,GDL|CH} = 6.62 \times 10^{-3} \sinh\left(0.003 \cdot p_{cap}\right) \tag{27}$$

Table 6
Thermal conductivity values of the MEA layers.

Property	[Units]	Equation	Reference
k_{th}	$[\mathrm{W m^{-1} K^{-1}}]$	$(1-\varepsilon)k_{th,solid} + \varepsilon\left[(1-s)k_{th,gas} + s k_{th,liq}\right]$	[23,61]
		$k_{th,solid} = \begin{cases} 0.16\ \frac{W}{mK}\ in\ GDL_{a/c} \\ 0.16\ \frac{W}{mK}\ in\ MPL_{a/c} \\ 0.2\ \frac{W}{mK}\ in\ CL_{a/c} \end{cases}$	
		$k_{th,gas} = \begin{cases} 0.03\ \frac{W}{mK}\ at\ cathode \\ 0.21\ \frac{W}{mK}\ at\ anode \end{cases}$	
		$k_{th,liq} = 0.65\ \frac{W}{mK}$	
$k_{th,MEM}$	$[\mathrm{W\ m^{-1} K^{-1}}]$	$0.177 + 3.7 \times 10^{-3}\lambda$	[62]
R_{th}	$[\mathrm{m^2\ K\ W^{-1}}]$	$\frac{d_{CV}}{2k_{th}}$	

Table 7
Source terms in the different domains of the model.

Domain	s	λ	O_2	H_2	N_2	H_2O	Heat
GDLc	S_{vl}	–	–	–	–	$-S_{vl}$	$S_{vl}\Delta\widetilde{H}_{vl} + f_{th} R_{el} i^2$
MPLc	S_{vl}	–	–	–	–	$-S_{vl}$	$S_{vl}\Delta\widetilde{H}_{vl} + f_{th} R_{el} i^2$
CLc	S_{vl}	S_d	S_{O_2}	–	–	$-S_{vl} - S_d$	$(S_{vl}+S_{vd})\Delta\widetilde{H}_{vl} + \left(-\Delta\widetilde{H}_{ORR} + \Delta\widetilde{H}_{vl} - 2F\left(\Delta\varphi_c - R_{CL}^{eff} i\right)\right)\frac{i}{2F}$
MEM	–	–	–	–	–	–	$R_{MEM}\, i^2$
CLa	S_{vl}	S_d	–	S_{H_2}	–	$-S_{vl} - S_d$	$(S_{vl}+S_{vd})\Delta\widetilde{H}_{vl}$
MPLa	S_{vl}	–	–	–	–	$-S_{vl}$	$S_{vl}\Delta\widetilde{H}_{vl} + f_{th} R_{el} i^2$
GDLa	S_{vl}	–	–	–	–	$-S_{vl}$	$S_{vl}\Delta\widetilde{H}_{vl} + f_{th} R_{el} i^2$

3.2. Along-the-channel model

Mass, energy and liquid water transport equations are solved along-the-channel direction in each of the CVs in which cathodic and anodic gas channels are discretized.

3.2.1. Transport of gaseous species

Mass conservation equation is solved according to Eq. (28):

Table 5
Reaction kinetics and charge transport properties.

Property	Units	Equation	Reference
$K_{r,ORR}$	$[\mathrm{mol\ m^{-2}\ s^{-1}}]$	$K_{r,ORR}^{*} \exp\left(-\frac{\alpha_{r,ORR} F}{\mathscr{R}}\left(\frac{1.1805}{353.15} - \frac{E_{0,ORR}}{T}\right) - \frac{42000}{\mathscr{R}}\left(\frac{1}{T} - \frac{1}{353.15}\right)\right)$	
$K_{r,PtO}$	$[\mathrm{mol\ m^{-2}\ s^{-1}}]$	$K_{o,PtO} \exp\left(\frac{2\,\mathscr{R}\,TE_{0,PtO}}{\alpha_{r,PtO} F}\right)$	[49]
$E_{0,ORR}$	[V]	$1.229 - 8.5 \times 10^{-4}\,(T - 298.15)$	[23]
σ_{ion}	$[\mathrm{S\ m^{-1}}]$	$\left[\sigma_{res} + \kappa_{ion}\left(f_v(\lambda) - f_v(\lambda_{th})\right)^{1.5}\right] \cdot \exp\left(\frac{10540}{\mathscr{R}} \cdot \left(\frac{1}{303.15} - \frac{1}{T}\right)\right)$	[23]
R_{MEM}	$[\Omega\ \mathrm{m^2}]$	$\sum_{i=1}^{n_{cv}} \frac{d_{MEM}/n_{cv}}{\sigma_{ion,i}}$	
HFR	$[\Omega\ \mathrm{m^2}]$	$R_{MEM} + R_{el}$	
R_{CL}^{eff}	$[\Omega\ \mathrm{m^2}]$	Eq. (24)	[23]
R_{el}	$[\Omega\ \mathrm{m^2}]$	Table A1	

Table 8
Boundary conditions for the through-MEA direction.

Domain Interface	Boundary conditions
CLa/c - MEM	• Gaseous molar species flux $\dot{n}_{gas,i}$ equal to zero. •Continuity in water content, λ, as well as water flux in ionomer, $\dot{n}_d$, continuity. •Liquid water flux, $\dot{n}_{liq}$, equal to zero. •Temperature and heat flux, $\dot{q}$, continuity.
CLa/c – MPLa/c	•Gas concentration, c_i, as well as gaseous molar species flux continuity •Water flux in ionomer, $\dot{n}_d$, equal to zero. •p_{cap}, and liquid water flux, $\dot{n}_{liq}$, continuity. •Temperature and heat flux continuity.
GDLa/c – MPLa/c	•Gas concentration, c_i, as well as single diffusive species flux continuity. •p_{cap} and liquid water flux, $\dot{n}_{liq}$ continuity. •Temperature and heat flux continuity.
GDLa/c – CHa/c	•Gaseous molar species flux at channel/GDL interface given by Eq. (29). •Heat flux continuity. •Liquid flux proportional to local p_{cap} (Eq. (27))

$$\frac{d}{dt}\left(V_{CH}^{j}\frac{p_i}{\mathscr{R}T}\right)=\dot{N}^{j,IN}\,y_i^{j,IN}-\dot{N}^{j,OUT}\,y_i^{j,OUT}+\dot{n}_{i,\mathrm{GDL|CH}}^{j}A_{MEA,CV} \tag{28}$$

where $\dot{N}^{j,IN}$ and $\dot{N}^{j,OUT}$ are the inlet and outlet molar flux in channel volume and $y_i^{j,IN}$ and $y_i^{j,OUT}$ are the mole fraction of species i at the inlet and outlet of the channel segment j, respectively. The unknown of Eq. (28), i.e. the mole fraction $y_i^{j,OUT}$, is calculated guaranteeing that the mole fraction in the centre of the j-th channel segment, y_i^j, is the average of inlet and outlet mole fractions, i.e. $y_i^j=\frac{y_i^{j,IN}+y_i^{j,OUT}}{2}$, as shown in Fig. 3. Therefore, $y_i^{j,OUT}=2{\cdot}y_i^j-y_i^{j,IN}$, where the mole fraction at the inlet of the j-th channel, $y_i^{j,IN}$, instead, is equal to the mole fraction of the gas coming from the previous channel segment, i.e. $y_i^{j,IN}=y_i^{j-1,OUT}=2{\cdot}y_i^{j-1}-y_i^{j-1,IN}$. $\dot{n}_{i,GDL|CH}^{j}$ in Eq. (28) is the molar flux of species i with respect to $A_{MEA,CV}$, entering the GDL/CH interface, assumed to be positive as it exits from GDL and enters the channel volume.

$$\dot{n}_{i,GDL|\mathrm{CH}}^{j}=h_{m,i}^{eff,j}\left(c_{i,GDL|\mathrm{CH}}-c_{i,\mathrm{CH}}\right) \tag{29}$$

with $h_{m,i}^{eff,j}$ as the effective gas convective mass transport coefficient (Eq. (36)).

The outgoing flow rate $\dot{N}^{j,OUT}$ from each CV is driven by the pressure gradient, calculated as in Ref. [19]:

$$\frac{p^{j+1}-p^{j}}{d_{CV}}=-\frac{f\,\mu_{gas}}{2\,d_h^2}\frac{\dot{N}^{j,OUT}}{\frac{p^j}{\mathscr{R}T}w_{CH}h_{CH}n_{RIB}} \tag{30}$$

where d_h is the hydraulic diameter of the channel and f is the friction factor expressed in Ref. [19]. To solve mass balance in gas channel some boundary conditions must be fixed: inlet mole fractions are set with Dirichlet-type boundary conditions, while the entering flow rate are given by

$$\dot{N}^{IN}=\begin{cases}\dfrac{i\,A_{MEA}}{4F}y_{O_2}^{IN}ST_c\\[2ex]\dfrac{i\,A_{MEA}}{2F}y_{H_2}^{IN}ST_a\end{cases} \tag{31}$$

where $ST_{a/c}$ are the anode and cathode stoichiometric ratio respectively.

3.2.2. *Transport of liquid water in channels*

During typical PEMFC dynamic operation, water management is furtherly complicated by the flooding of gas channel, especially at the cathode side [63,64]; cell performance and mass transport are highly affected by liquid water in channels and, particularly, by its flow pattern [65]. Under high current density, a large number of droplets emerging from GDL aggregate in the channel giving rise to water film that might hinder mass transport [66]. Water balance in gas channel volume must be correctly investigated, especially under transient operation of the fuel cell [67]. A liquid channel saturation, s_{CH}, was defined as the channel volume fraction occupied by liquid water [68,69] and the resulting governing equation is:

$$\frac{d}{dt}\left(\frac{\rho_{liq}}{M_{H_2O}}s_{CH}^{j}\,V_{CH}^{j}\right)=\frac{\rho_{liq}}{M_{H_2O}}v_{liq}s_{CH}^{j-1}h_{CH}w_{CH}-\frac{\rho_{liq}}{M_{H_2O}}v_{liq}s_{CH}^{j}h_{CH}w_{CH}+\dot{n}_{liq,GDL|CH}^{j}A_{MEA,CV} \tag{32}$$

The first and second terms on the right-hand side of Eq. (32) represent respectively the liquid water fluxes entering and exiting from the channel segment, dependent upon liquid velocity v_{liq}, resulting from the balance of strains acting on the liquid film and droplets [70,71]. Neglecting the gravitational force, whose contribution is one order of magnitude lower the others for horizontal channels [70], the adhesion, shear and pressure drop related forces affect the motion of liquid droplets inside channels. The former represents the resistance force a droplet needs to overcome to initiate motion along the surface and it

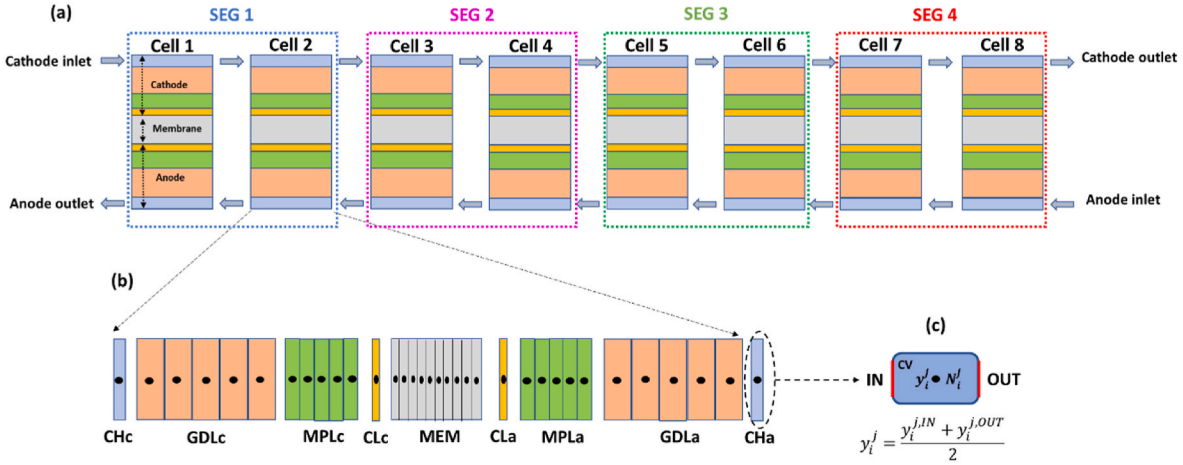

Fig. 3. (a) Representation of the eight regions used as computational domain, (b) control volume (CV) approach used to discretize the through-MEA direction, determining one MEA model segment, (c) CV approach used to model cathodic and anodic gas channels. Each of the four experimental segment of the segmented hardware is discretized using two MEA model segments.

does not depend on the velocity field in the channel [72], whereas the shear strain, determined by the fluid shear along the liquid surface [71], and the pressure strain, generated by the pressure gradient along the channel segments, depend linearly on the flow velocity in gas channels [72]. Since this model aims at capturing the effect of liquid water on the mass transport, the following simplified correlation is proposed, lumping the effect of the forces described above.

$$v_{liq} = \alpha_{liq}\, v_{gas} = \frac{\alpha_{liq}}{1-s} v^{*}_{gas} \tag{33}$$

where v_{gas} and v^{*}_{gas} are the actual and superficial gas velocity respectively. The geometry of the flow field strongly affects water removal: as stated in Ref. [73], due to smaller pressure drop and poorer gas flow, water removal is more difficult in parallel flow field with respect to serpentine flow field. Therefore, the parameter α_{liq} was calibrated on the experimental data to realistically account for the effect of flow field geometry.

3.2.3. Convective mass transport resistance at gas channel-GDL interface

The gas convective mass transport coefficient in the channel is determined for each species:

$$h_{m,i} = \frac{Sh_i \cdot D_i^{mix}}{d_h} \tag{34}$$

where d_h is the channel hydraulic diameter and D_i^{mix} is the molecular diffusivity of the i species in the mixture, computed according to Table 2. Sh_i is the Sherwood number of the i species, which is commonly expressed as a function of the Reynolds number and the Schmidt number, Re and Sc_i [74]:

$$Sh_i = 1.615 \cdot \left(\frac{d_h}{z_{ch}} Re \cdot Sc_i\right)^{1/3} \tag{35}$$

Liquid water presence in channel is significantly impacting mass transport in two ways: on one side, it is hindering, at most blocking, species mass transport towards cathode GDL; on the other one, it can strengthen gas convection by decreasing channel cross section area. The combined effect determines a fluctuating oxygen concentration in cathode CL and the relative impact of the two effect is dependent upon the liquid flow pattern [75]. For the case of a film flow, the blocking effect is reported to be dominant, determining an initial decrease in the oxygen concentration, followed by a slow increase, as liquid water is discharged from the channel [65]. In Ref. [76], the oxygen concentration drops at the interface between GDL and gas channel was expressed in terms of effective Sherwood number. It was thus assumed to reduce mass transfer coefficient by an additional contribution dependent on the channel saturation, s_{CH}, through a constant parameter, κ_{liq}:

$$h^{eff}_{m,i} = \left(\frac{1}{h_{m,i}} + \kappa_{liq} s_{CH}\right)^{-1} \tag{36}$$

3.2.4. Heat transport

Energy conservation equation must be solved both for gaseous species, at anode and cathode sides.

$$\frac{d}{dt}\left(C_{th,CHc} V^{j}_{CHc} T^{j}_{CHc}\right) = \left(\dot{q}^{j}_{GDLc|CHc}\right)(w_{CH} + w_{RIB}) d_{CV} - \dot{N}^{j,OUT}_{CHc} c_p \left(T^{j}_{CHc} - T_{ref}\right) + \dot{N}^{j,IN}_{CHc} c_p \left(T^{j-1}_{CHc} - T_{ref}\right) \tag{37}$$

$$\frac{d}{dt}\left(C_{th,CHa} V^{j}_{CHa} T^{j}_{CHa}\right) = \left(\dot{q}^{j}_{GDLa|CHa}\right)(w_{CH} + w_{RIB}) d_{CV} - \dot{N}^{j,OUT}_{CHa} c_p \left(T^{j}_{CHa} - T_{ref}\right) + \dot{N}^{j,IN}_{CHa} c_p \left(T^{j-1}_{CHa} - T_{ref}\right) \tag{38}$$

Where $C_{th,CHc/a}$ is the heat capacity of cathodic or anodic gas channels and $\dot{q}^{j}_{GDL|CH}$ is the heat flux evaluated at both anode and cathode GDL and channel interfaces. Inlet temperature is set for the inlet fluxes and on the outer faces of the BPs. The reference temperature, T_{ref}, is equal to 353.15 K.

3.3. 1+1D PEMFC model: numerical implementation

According to the method previously introduced, the system of governing equations is implemented into a 1+1D domain, discretized into a certain number of CVs, as in Fig. 3. The along-the-channel direction is discretized into 8 CVs, whereas the through-plane direction presents 5 CVs for each GDL, 5 CVs for each MPL, 1 CV for each CL and 10 CV for membrane. The number of CVs adopted for each sub-domain resulted from a sensitivity analysis, aimed at saving computational time and being physically consistent. The cell active area attributed to each CV, $A_{MEA,CV}$, in the along-the-channel direction from the first to the eighth is equal to 2.92 cm^2, 2.92 cm^2, 2.90 cm^2, 2.90 cm^2, 3.82 cm^2, 3.82 cm^2, cm^2, 2.86 cm^2 and 2.86 cm^2, where each of the four segments of the experimental segmented hardware is discretized using two MEA blocks.

As it is shown in Fig. 3, “Cell 1” coincides with cathode inlet and anode outlet while “Cell 8” corresponds to cathode outlet and anode inlet. Therefore, at “Cell 1” all the boundary conditions related to cathode feed, i.e. mass flow rate, inlet temperature, inlet pressure and inlet relative humidity are imposed, while at “Cell 8” all the boundary conditions concerning anode feed are fixed. Considering that cell voltage is equal among the 8 different MEA segments, the preset ode15s solver implemented in MATLAB-Simulink environment iteratively solves for each time step and in each point of the domain the system of the equations, such that the global current density is equal to the one imposed externally, changing the cell voltage. Relative and absolute tolerances of the solver were fixed to 1×10^{-9}. For solving the liquid water transport in porous media, a minimum is considered for the liquid relative permeability, specifically 5.12×10^{-7}, to avoid numerical instabilities.

Polarization curve simulations and limiting current density simulations were performed by applying the same experimental profile, as described in Section 2. For the driving cycle operation, the Low-Power operation and the High-Power operation, with the experimental boundary conditions, shown in Fig. 1, were simulated without including the short-stop procedure, as performed experimentally [25].

3.4. Methodology for model calibration and validation

The 1+1D PEMFC model described in Sections 3.1 and 3.2 is calibrated and validated on a wide set of experimental data gathered on the segmented cell hardware described in Section 2. In particular, local polarization curves, whose operating conditions are listed in Table 1, global limiting current tests and a dynamic cell voltage response to a current step are exploited to calibrate the model. Model validation, instead, exploits experimental data representative of real cell operation under the ID-FAST drive cycle protocol, distinguishing between the Low-Power and the High-Power operating mode of the load cycle, previously described in Section 2, together with local experimental data from limiting current density test. Furthermore, to furtherly proves the predictive capabilities of the model, the effect of air inlet humidification was also investigated by comparing model simulations with experiments. A statistical index, the root mean square error (RMSE), is provided where necessary to prove the consistency between model simulations and experiments. The main results of model calibration and validation are discussed in Sections 4.1 and 4.2 respectively.

4. Results & discussion

4.1. Model parametrization and calibration

The 1+1D PEMFC model is calibrated on the experimental data described in Section 2. For this purpose, a specific dataset is considered, including polarization curves (Table 1), limiting current tests and voltage dynamic response under current step, evaluated in the same operating conditions of driving cycle load protocol. Parameters values were taken from the literature whenever possible or known but, nevertheless, a set of 10 parameters was identified to require calibration based on their uncertain nature or on a sensitivity analysis. Those parameters were proven to have significant effect on model predictions, affecting the kinetic, ohmic and mass transport overpotentials, as also observed in the literature [77–79]. The values are reported in Table 9 and commented in this section. In Table A1, in the Appendix, all the model parameters are shown. The parameters are discussed in groups to separate those related to ORR kinetics, those affecting ionic conductivities and those impacting both on gas and liquid water transport.

Parameters affecting ORR kinetics are the rate constant $K^{*}_{r,ORR}$, which is then corrected to account for its temperature dependence, and the platinum oxidation rate constant, $K_{o,PtO}$. The former was calibrated from the low current density region of the "oxygen" polarization curve, determining a value equal to 1452 mol m^{-2} s^{-1}, in the typical range from literature [80]. Since the evolution in time of oxide coverage profile, as well as its dynamic growth or reduction, is crucial if the aim is to accurately model the transient performance of a PEMFC [23,81], it was decided to calibrate the platinum oxidation rate constant, $K_{o,PtO}$, from a dynamic test. In particular, the model voltage response to two current steps, from 0.59 to 0.25 A cm^{-2} and from 0.25 to 0.095 A cm^{-2}, shown in Fig. 4, was analysed and compared to experiments. $K_{o,PtO}$ was found to be equal to 2×10^{-10} mol m_{Pt}^{-2} s^{-1}, which is in accordance with typical kinetic constant related to PtO formation, implicitly corrected by the Temkin factor [81,82]. The other parameters of electrochemical ORR and HOR reaction kinetics are based on literature values [55].

Parameters that determine the ion conductivity in the membrane and the catalyst layers, thus related to σ_{ion}, are the coefficients σ_{res}, κ_{ion} and λ_{th}. These parameters were calibrated on local polarization curves under "reference" and "dry" conditions, focusing on the ohmic region of the same. Good fit values were proven to be 0.3 S m^{-1}, 50 S m^{-1} and 1 respectively, which are within the acceptable range reported in Ref. [23].

Parameters affecting gas transport were estimated through limiting current test. In particular, Knudsen radii for MPLs and CLs were calibrated, together with the factor f_{land} which, as it was already discussed in Section 3.1.2, is used to increase the diffusion path of the species in the GDL to accounts for the effect of the land structure on the transport process. Under low oxygen concentration and flow rate, no effect of liquid transport on mass transport is expected, confirmed by model predictions and consistent with [77].

On the contrary, liquid transport parameters, specifically α_{liq} in Eq. (33) and the specific mass transport resistance associated to the presence of a liquid film, κ_{liq}, in Eq. (36), were fitted by focusing on the mass transport region of the "reference" polarization curve which, due to its fully humidified operating condition, is the one that shows the most critical liquid water removal. It should be noted that the resulting liquid velocity values during simulation of the "reference" polarization curve is consistent with values reported in Ref. [83], in the order of $1 - 2.5 \times 10^{-3}$ m s^{-1}.

In Fig. 4, the voltage response to specific current steps is reported and good adherence with experimental data is observed. Cell voltage is slightly overestimated with respect to the experimental signal, particularly in the first 20 s after the second step, even if the characteristic time of voltage relaxation is consistent with experimental trend. This peculiarity can be ascribed to the simplified approach used in the description of Pt-oxide formation/reduction equation. Pt-oxide layer growth is an electrochemical process which might be characterized by several intermediate steps and involve different oxide species and their characteristic times are actually different, depending upon the species [84]. In this model, the coverage caused by PtOx species is modelled with a single reaction mechanism, as done in previous literature [81]. The discrepancy with experimental data suggests that some oxide species are formed in a short time while a different type of oxide is formed under longer time scale, as discussed in our previous work [85]. This could explain the reason why discrepancies in terms of amplitude of voltage peaks can be detected.

Fig. 5 shows a comparison between model results and experimental data in terms of polarization curves: in each plot curves recorded in each segment are reported from air inlet, Fig. 5(a), to air outlet, Fig. 5(d). Local cell performances are well predicted in a wide range of operating condition (different relative humidities and stoichiometries). For the "dry" polarization curve, an improvement in performance is visible, moving along the channel direction, thanks to the better ionomer hydration, whereas, for the "reference" condition, a decreasing trend in performance is evident, passing from the cathode inlet region to the outlet one. For the fourth segment, corresponding to cathode outlet, a decay in performance is observed for the high-current density region, caused by mass-transport resistances induced by liquid water flooding of porous media and channel. For the inlet segment, in the "dry" polarization curve, an underestimation of performance is visible, mainly for intermediate and high current density values, associated to higher predicted ohmic losses. Indeed, in the low RH conditions, because of proton-transport limitations, it is expected that the ORR reaction takes place mostly in the region of the cathode CL near the membrane. The lumped model of CL may slightly overestimate the effective resistance to proton transport under dry conditions, because of its simplified assumptions. A good consistency is anyway obtained after model calibration.

Global limiting currents values, evaluated as a weighted average of local segments performance, were used for calibration purposes and they are reported in the SI. In Fig. 6, local limiting currents for three different oxygen dilution, 1%, 2% and 3%, are shown as model validation, to firstly prove the capability of the model to predict performance heterogeneities. Because of the largest oxygen activity, the cathode inlet, namely segment number 1, is the best performing region of MEA and, proceeding in the along-the-channel direction, a significant performance reduction is observed due to the progressive oxygen depletion. This holds true also increasing oxygen dilution up to 3 %.

Electrochemical impedance spectroscopy was also simulated to evaluate the consistency between conductivity values in the model and in the experiment and it is reported in the SI. Because of the simplification in the description of the cathode catalyst layer, few differences are observed between the simulated and the experimental spectra, which cannot thus be used for direct calibration. Nevertheless, it proves good capability of the model to separate Ohmic and kinetic phenomena.

Table 9
Model parameter calibration.

Parameter	Units	Value	Source
σ_{res}	[S m^{-1}]	0.3	Polarization curves
κ_{ion}	[S m^{-1}]	50	Polarization curves
λ_{th}	[−]	1	Polarization curves
$K^{*}_{r,ORR}$	[mol m^{-2} s^{-1}]	1452	Polarization curves
$K_{o,PtO}$	[mol m^{-2} s^{-1}]	2×10^{-10}	Current step response
f_{land}	[−]	1.4	Limiting current
α_{liq}	[−]	9.5×10^{-4}	Polarization curves
κ_{liq}	[s m^{-1}]	350	Polarization curves
$r_{Kn,CLa/c}$	[nm]	250	Limiting current
$r_{Kn,CLa/c}$	[nm]	70	Limiting current

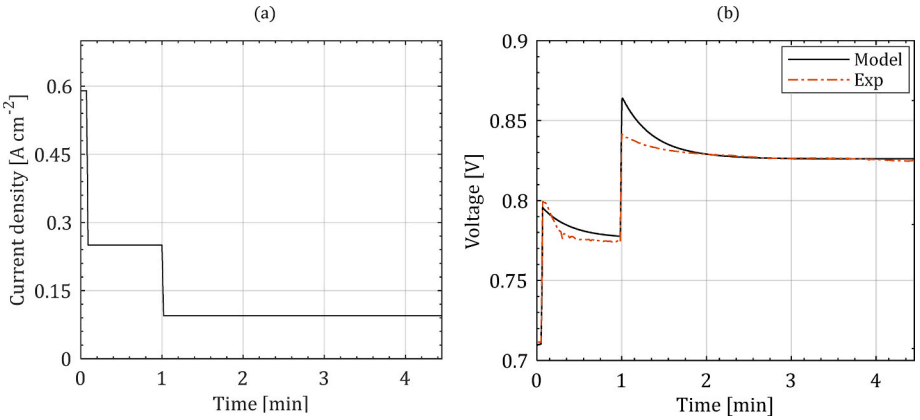

Fig. 4. – (a) Two consecutive current down-steps, from 0.59 to 0.25 A cm^{-2} and from 0.25 to 0.095 A cm^{-2}, under the operating conditions of driving cycle. (b) Experimental (dashed line) and simulated (solid line) voltage dynamics response to the current down-steps.

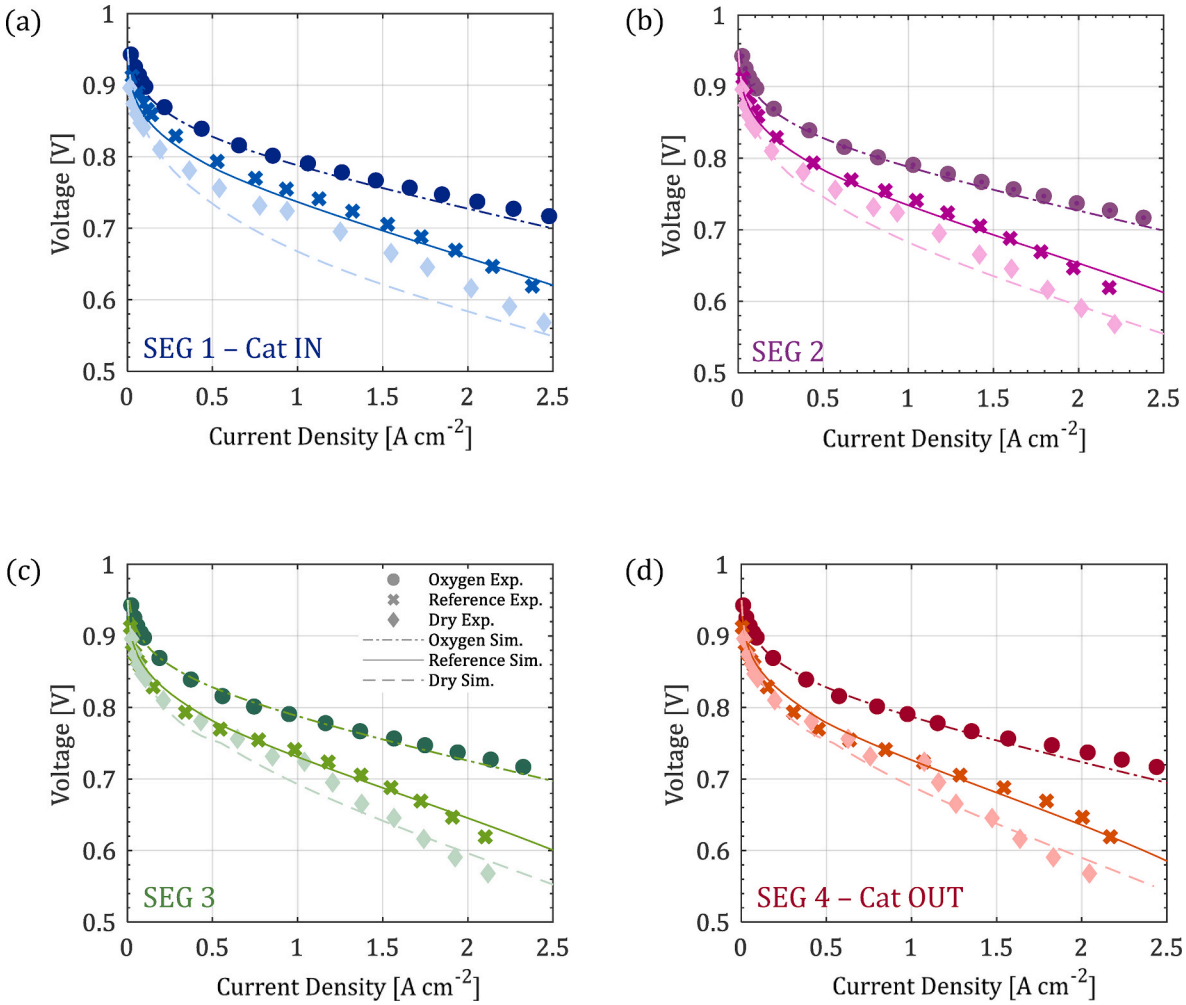

Fig. 5. Model calibration on local polarization curves whose operating conditions are listed in Table 1. Markers refer to experiments, lines to model results.

4.2. Model validation

4.2.1. Analysis of Low-Power operation

The ID-FAST driving cycle, described in Section 2, was simulated with the 1+1D PEMFC model described and calibrated in previous sections. Fig. 7(a) shows a comparison between model predictions and experiments in terms of voltage profile during Low-Power, demonstrating adherence with experimental data, as confirmed also by the root mean square error (RMSE) that is equal to 7.9 mV. Slow voltage dynamics can be observed and it is attributable to the combination of physical phenomena with higher characteristic time, specifically platinum oxide layer formation and ionomer hydration in catalyst layers and membrane. In SI, further insights are reported showing how PEMFC dynamic performance at local and global level are singularly affected by these two phenomena. Pt-oxide surface coverage is reported in Fig. 7(b) and, as in Fig. S8, it can be inferred that downward and upward cell

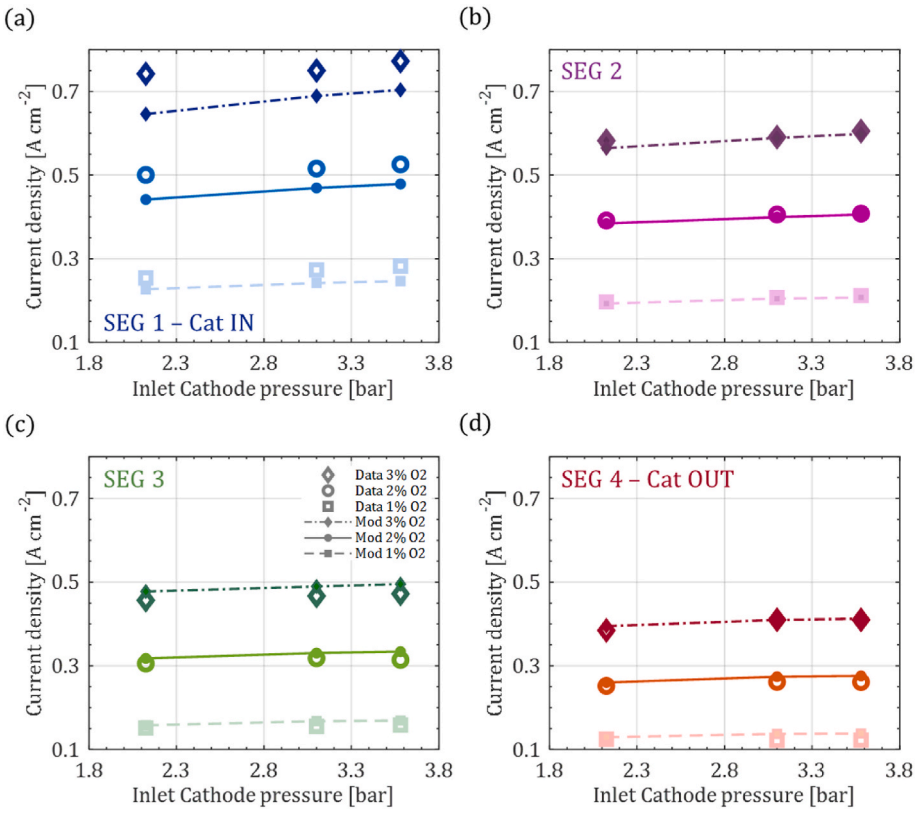

Fig. 6. Local limiting current test. Measurements are carried out for three different values of oxygen dilution: 1 %, 2 % and 3 %. Squares, circles and diamonds refer to experiments and to an oxygen dilution equal to 1 %, 2 % and 3.

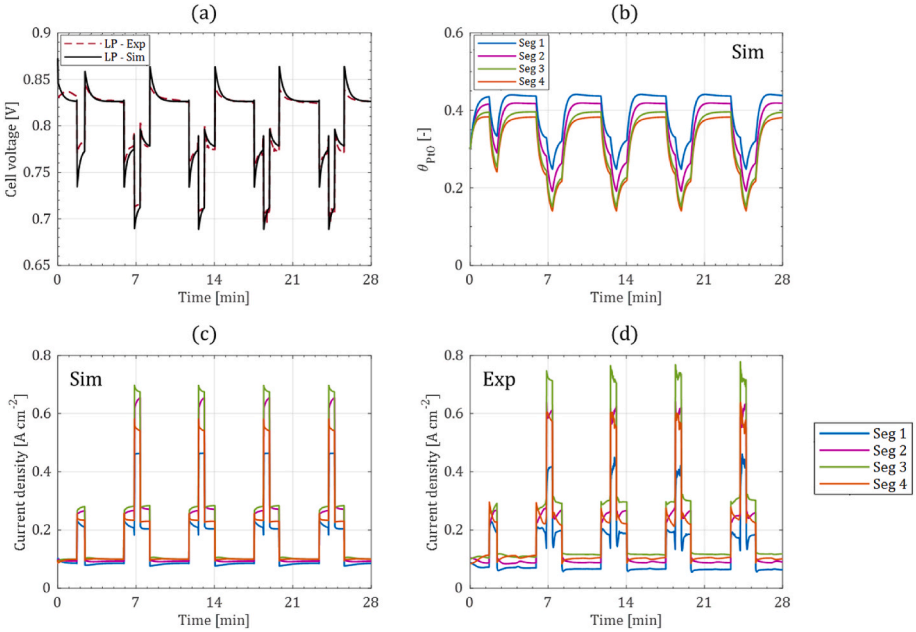

Fig. 7. – Low-Power operation: (a) Simulated and experimental voltage. (b) Predicted PtO coverage (c) Simulated and (d) experimental local current density evolution for the four segments.

voltage peaks are attributable for a large extent to such dynamics. The small discrepancies in terms of amplitude of cell voltage peaks are ascribable to the simplified description of PtO formation. Nevertheless, during the driving cycle, ϑ_{PtO} ranges between 0.1 and 0.45, consistently with other values reported in literature for the same range of potential [23]. It is worth also noting that, consistently with the physics of the phenomenon, the fraction of active surface covered by platinum oxide, as current increases, starts decreasing, explaining partially voltage undershoot, and it does not reach a stabilization in 50 s. The same holds true, going lower in current, at 0.59 A cm^{-2}. As current lowers again, determining an increase in cathode potential, ϑ_{PtO} starts increasing again, causing the overshoot in cell voltage. For the low-current period

at 0.095 A cm^{-2}, lasting 180s, the oxide coverage shows after a fast increase, a relaxation period, determined by the simultaneous decrease in cell voltage. From Fig. 7(b) it can also be appreciated that the PtO surface coverage slightly changes among the four different regions of the MEA, consistently with local operating conditions: indeed, because of the lowest water content, it will be better explained later, segment 1 experiences the highest ohmic losses and, therefore, at fixed voltage produced by the four regions of the cell, it will be characterized by the highest cathode electrode potential, which promotes the formation of an oxide layer on platinum nanoparticles surface.

Fig. 7(c) and (d) provides the along-the-channel distributions of current density according to simulation and experiments respectively, by which it can be detected the ability of the model to correctly predict how performance vary among the four different sections of the cell. To quantify the coherence between model simulations and experiments in terms of local current density, the average RMSE among the four different MEA portion is calculated and it results equal to 20 $mA/\ cm^2$ meaning that, in the Low-Power operating conditions of the ID-FAST protocol, the proposed model is capable to correctly reproduce performance heterogeneity. Further information concerning the local RMSE of the four different cell segments can be found in the Supplementary Information. Consistently with experimental behaviour, the third segment of the MEA is found to be the most performing one, whereas cathode inlet region is actually characterized by the worst performance, under all the operating conditions of the Low-Power region. The main driver for performance is represented by the hydration state of the ionomer in cathode catalyst layer, reported in Fig. 8(c). The ionomer hydration is actually increasing along channel direction, because of water accumulation along the channel and the simultaneous higher water production, demonstrated by the middle region. Indeed, the third segment is experiencing the largest water content λ, determining very low ohmic losses and thus, higher performance, although oxygen activity is lower. The cathode-outlet region, although a relevant water content, as shown by Fig. 8(c), is less performing than cathode-middle region because of the lower oxygen activity related to the progressive consumption of reactants along the channel and to larger liquid water fraction in porous media, as shown by Fig. 8(d). Cathode inlet region, instead, presents an average λ equal to 3–4, that is actually impacting on proton transport, determining higher ohmic losses both in membrane and cathode CL.

Focusing on current redistribution among segments, current dynamics of the different regions are well reproduced for all the current density range. Looking at 0.59 A cm^{-2}, the third and the fourth segments present a decreasing trend in current density, ascribable to a decrease in oxygen activity, whereas the first and the second segments tend to perform better, thanks to better hydration. On the other side, as visible in Fig. 8(d) and (e), reporting the evolution of liquid saturation in both cathode CL and channel during the Low-Power period, both the third segment and the fourth segment presents an increasing average saturation, ranging between 2 % and 3 %, during 0.59 A cm^{-2}, that hinders oxygen transport towards GDL and through the CL.

A further insight into understanding the hydration state of the MEA along channel direction is given by the analysis of the HFR (Fig. 8(a) and (b)). During this part of driving cycle, an important reduction of HFR can be observed passing from the first to the fourth segment, consistently with the progressive water generation and accumulation along gas channel volumes, as also demonstrated by the hydration state of cathode ionomer and testifying the good reproduction of water dynamics. The experimental HFR is reported for comparison and a good consistency with the simulated value, ranging from 90 mΩ cm^2 to 20 mΩ cm^2. For the fourth segment, a slightly higher value is predicted, determined by a decrease in water content in the very outlet region. This is linked to an underestimation of water saturation at cathode outlet that is expected to be higher in real world flow channels, under the same operating conditions [86]. Lastly, it must be pointed out that there is a significant

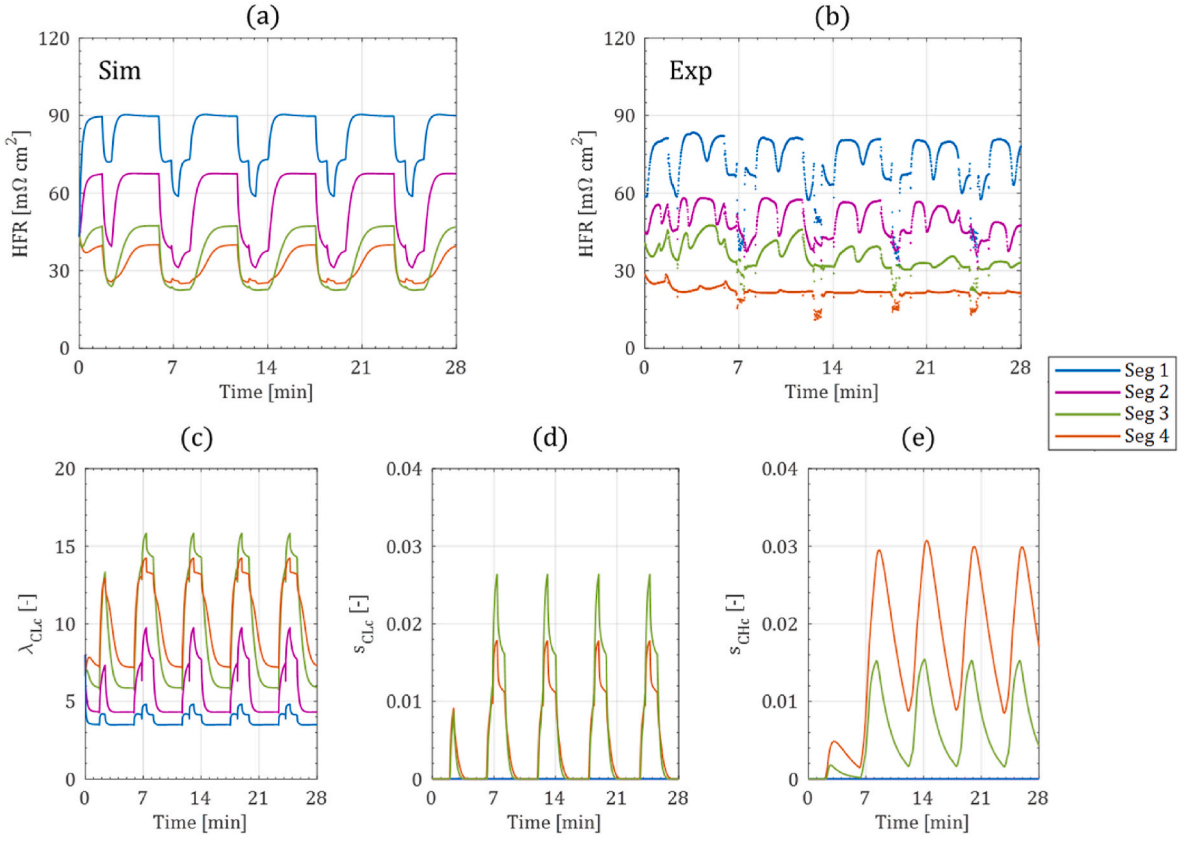

Fig. 8. – Low-Power operation: Simulated (a) and experimental (b) HFR distribution among the different segments. (c) Predicted water content at cathode CL for the four segments. (d) Predicted liquid saturation at cathode CL for the four segments. (e) Predicted liquid saturation along the cathode channel for the four segments.

change in the hydration state among cell segments from cathode inlet to cathode outlet, and the continuous cycling, mainly at lower hydration state, could be particularly detrimental for ionomer durability, linked to mechanical stresses.

4.2.2. Analysis of High-Power operation

In Fig. 9(a), simulated voltage profile during the High-Power period, is compared with the experimental one, showing a consistent prediction of the same. The root mean square error, indeed, is equal to 22 mV. Load is dynamically changing, together with the simultaneous change in operating pressure, temperature and dew point of the feed gases, and this causes significant voltage transients, that are actually ascribable to local mass-transport related phenomena.

As already seen for the Low-Power operation, ϑ_{PtO} is varying over time but its impact on ORR is actually lower with higher loads, since oxide-free active area is higher. Specifically, during simulation of Low-Power operation, its variation ranges between 0.43 and 0.25, whereas during High-Power operation, it varies between 0.2 and 0.09, apart from the first minutes, where it rapidly decreases from 0.43, following the fast load change. In Fig. 9(c) and (d), simulated and experimental local current density distribution is shown. It is actually decreasing along cathode channel, with the cathode inlet region that is the best performing one at 1.75 A cm^{-2}. Indeed, as visible in Fig. 10(c), proton transport is not the limiting phenomenon, because the higher water production, as well as higher RH in channels, is favouring the ionomer hydration. Thus, the main driver in local performance is represented by oxygen activity at cathode CL, that is progressively decreasing along channel direction. Mass transport is furtherly hindered by a higher liquid flooding of the porous media and channel volumes. As it is shown in Fig. 10(e), because of the highest liquid water saturation in cathodic gas channel, third and fourth segments of the cell are experiencing relevant flooding phenomena which significantly hinder reactant diffusion causing an important performance decay. Further analysis on the effect of channel flooding on PEMFC dynamic performance is present in SI. It is worth noting that also the cathode inlet region is characterized by a certain degree of flooding during this operation regime, even if with a minor intensity with respect to middle-outlet region. For all the segments of the cell, the increase of liquid saturation in channel at increasing current output, up to the maximum load value, namely 1.75 A cm^{-2}, determines a significant increase of mass transport resistance in channel and hence a reduction in local performance, with a voltage undershoot around 0.62V. At the same time, the high mass flow rate, and hence high liquid phase velocity, proportionally linked to gas-phase one, allows water to be progressively discharged from the channel. This is also favoured by the simultaneous increase in cell temperature, that lets to keep more water in vapor phase, thus decreasing the magnitude of water flux exiting from the GDL, and by a lower RH of the air fed on the cathode side.

The drying phenomenon caused by an increasing cell temperature, and thus by a decreasing RH at cathode channel inlet, affects the predicted performance of the inlet region, whose current output, as it is evident by Fig. 9(c), starts suddenly decreasing reaching a downward peak at minute 62. This peculiar behaviour is less pronounced in the experimental data where current distribution of the different regions tends to converge. The discrepancy could be attributed to the underestimation of the local saturation, linked to an overestimation of the discharge capacity of the porous media and channel. The complex interconnection among the three phases of water inside MEA layer is still object of investigation and debate in PEMFC modelling and it has a strong impact on dynamic performance, particularly at a local level [87]. Moreover, the liquid water flow through channel could occur with different flow patterns and may be influenced by the gas-phase velocity field, by the wettability property of channel and GDL surfaces, as well as by the flow field geometry. Even if the two-fluid flow model

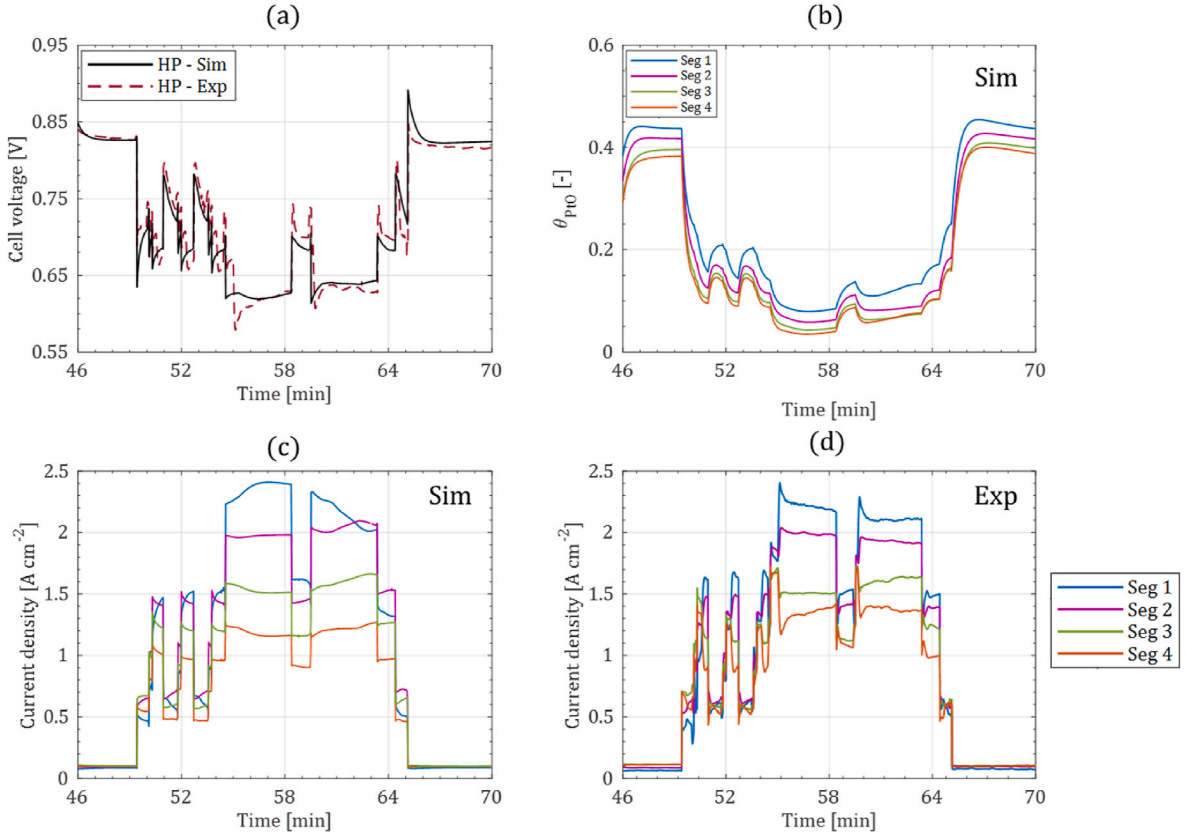

Fig. 9. – High-Power operation: (a) Simulated and experimental voltage. (b) Predicted PtO coverage (c) Simulated and (d) experimental local current density evolution for the four segments.

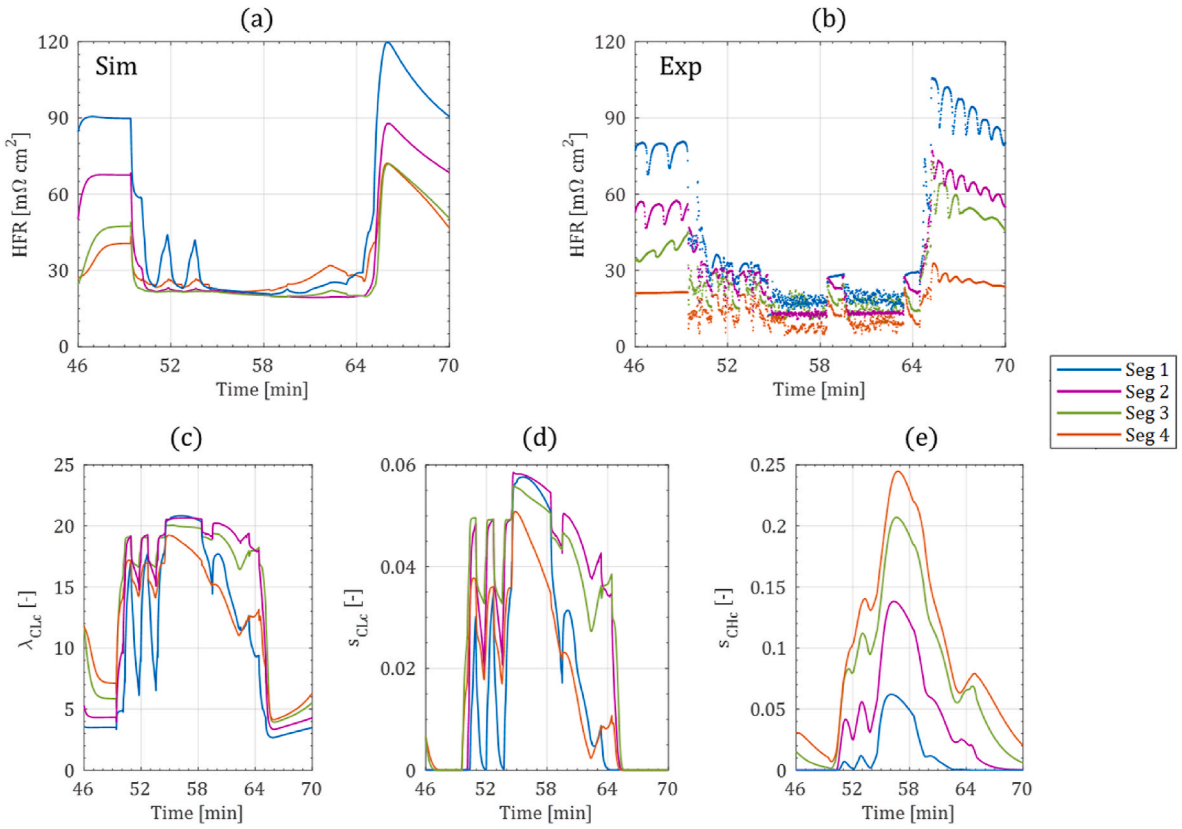

Fig. 10. – High-Power operation: Simulated (a) and experimental (b) HFR distribution among the different segments. (c) Predicted water content at cathode CL for the four segments. (d) Predicted liquid saturation at cathode CL for the four segments. (e) Predicted liquid saturation along the cathode channel for the four segments.

demonstrated to work well with steady-state conditions and to indirectly capture the effect of liquid water on MEA performance, on the other side, in a highly dynamic scenario, it could let to underestimate the actual liquid water saturation [88].

The average RMSE is higher in the High-Power mode ($112\ mA/cm^2$) with respect to the one estimated for the Low-Power region ($20\ mA/cm^2$). Here, the larger discrepancy, as already discussed above, is associated with the peculiar behaviour of the cathode inlet region of the cell and is also consistent with the higher measurement uncertainty under high current operation compared to low current. Furthermore, in comparing model simulations with experimental data, it must also be taken into account the intrinsic dynamics of the devices and equipment that make up the testing station, for instance gas humidifier and back pressure valves. The testing system components may induce uncontrolled phenomena, such as water condensation in pipes or the local formation of liquid water droplets, that may only in part or not at all described by a mathematical model and that may play an important role when testing a dynamic drive cycle on a real cell. Further details can be found in the Supplementary Information.

Looking at the HFR evolution over time during high load request period of the High-Power, the difference between segments is minor, with value around 17 mΩ cm^2 and 22 mΩ cm^2 because of the higher water production. It is, however, worth to analyse what is occurring in the last part of the High-Power operation, where load drops down from 1.75 A cm^{-2} to 0.095 A cm^{-2} and membrane and CLs ionomer actually experienced a drying-out period. It can be observed, looking at Fig. 10 (a), a significant rapid increase in the HFR, experienced by all the cell segments, followed by a slow decrease to the operating values of the Low-Power period. Specifically, the HFR of the inlet region, with the highest variation, is peaking at a value around 120 mΩ cm^2, followed by all the other segments proportionally with a minor intensity. The simulated dynamics is consistent with what observed experimentally, shown in Fig. 10(b). Similarly, the water content in the cathode CL ionomer shows a fast-decreasing trend with main impact on the inlet region. The presence of the peak is related to the superposition of different effects: high cell temperature, decreasing pressure and low water production. With load decrease, also water production is decreasing, determining a decrease in the local hydration state of the ionomer. The equilibrium water content of the ionomer is strongly related to the RH of the air around the ionomer film and, as pressure goes down, also the RH is expected to rapidly decrease, thus increasing the driving force for the desorption phase. This operating condition is worsened by high cell temperature, that keeps RH low. Actually, the consecutive rehydration of the ionomer is dominated by the dynamics of cell temperature, that keeps on decreasing, down to 71 °C. This phenomenon can occur during real-operation of automotive fuel cell system, as also reported in Ref. [89].

4.2.3. *Analysis of inlet air humidification*

To analyse the effect of air inlet humidification on PEMFC performance in single-cell, the Low-Power operation of the cycle was simulated considering two additional different values of air RH at channel inlet, namely 15% and 50%.

In Fig. 11, simulated and experimental voltage profile during Low-Power for the three different cases are shown. A reduction of the RH at cathode gas channel inlet determines a progressive worsening in stack performance resulting in a downward shift of voltage profile and, thus, of efficiency. Looking at the ionomer hydration, it actually gets reduced with lowering RH of air feed stream. Since during Low-Power simulation the limiting phenomena affecting PEMFC performance is represented by the proton transport across membrane and catalyst layers, thus it is not surprising to detect that the case RH-15 presents the lowest performance. This is also confirmed by the average stack efficiency, which decreases from 62.2% for the case RH-30 to 61.5% for the case RH-15.

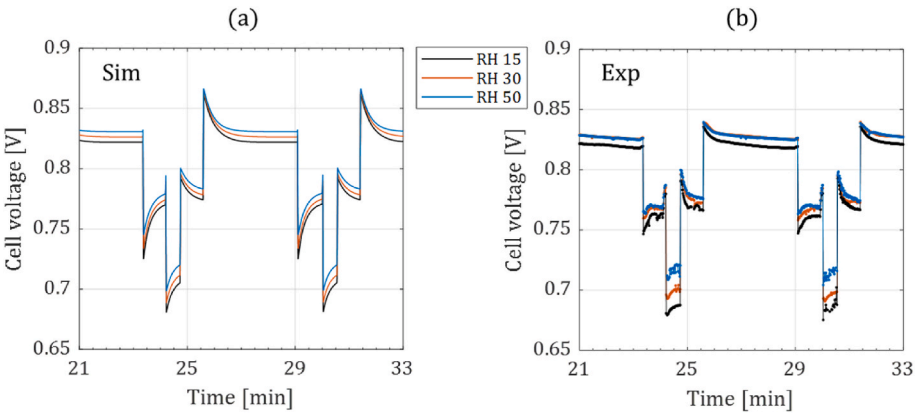

Fig. 11. – (a) Simulated and (b) experimental cell voltage during Low-Power operation for different RH.

According to experimental data, no relevant variations can be observed between case RH-30 and case RH-50, in the high-voltage region, whereas a slight increase in voltage is appreciable between those two cases at lower voltage, i.e. at 0.59 A cm^{-2}. Model is predicting slightly higher performance for the case RH-50, linked to a further increase in performance of the inlet region. Consequently, a slight improvement in the average stack efficiency, from 62.2% for the case RH-30 to 62.8% for the case RH-50, is predicted by the model. The effect of air inlet humidification on the local current density, for the cases RH-15 and RH-50, is reported in Fig. 12(a)–(c) respectively and compared with experimental results, Fig. 12(b)–(d). According to both experiments and model prediction, a progressive reduction in current output of cathode inlet region, i.e. segment 1, can be observed at decreasing RH of air feed stream. Indeed, the drier feed conditions get worse proton conductivity increasing, therefore, ohmic losses.

A progressive increase in current output of the third segment of the MEA on the contrary, can be observed at decreasing RH. This behaviour is the result of both a mathematical and physical phenomenon: indeed, at fixed current output required to the stack, if performance of cathode inlet region decreases thus, obviously, those of cathode outlet region must increase. Furthermore, thanks to water production by ORR, water is progressively accumulated along-the-channel and this works in favour of third and fourth segments which, therefore, exhibit a good hydration state that contributes to improve local performance. Thus, it is not surprising to detect that for the case RH-15 segment number 3 is the most performing one, even more than the fourth thanks to a larger oxygen activity. For the case RH-50 the situation is reversed in the sense that cathode inlet region, and in particular the segment 2, becomes more performing than cathode outlet region where the accumulation of liquid saturation in porous media, together with oxygen depletion, contributes to deteriorate local performance. Further details on the effect of inlet humidification may be found in the SI.

5. Conclusion

A 1+1D transient non-isothermal and multiphase PEMFC model has

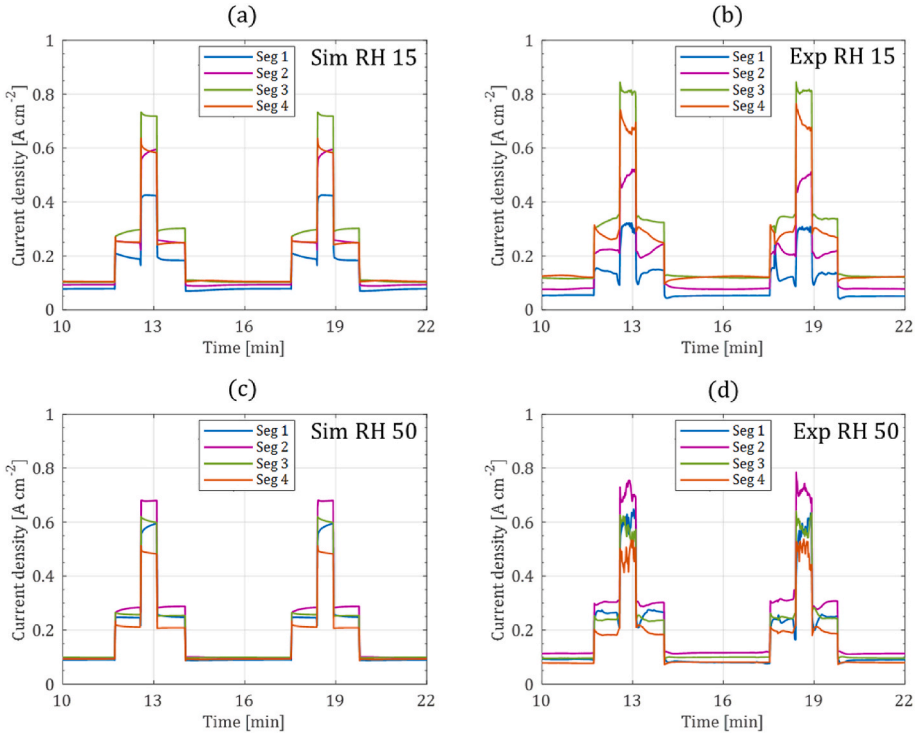

Fig. 12. – (a) Simulated and (b) experimental local current density for an air inlet humidification equal to 15 %. (c) Simulated and (d) experimental local current density for an air inlet humidification equal to 50 %.

been developed and implemented. It consists in a 1D through-the-membrane transport model, which accounts for all the main transport phenomena occurring in PEM fuel cells, i.e. gas and liquid phase transport in porous media, dissolved water phase transport through membrane, charge transport in catalyst layers and heat transport through the MEA, plus a 1D along-the-channel model that, solving both mass and heat balances, allows to accurately predict changes in reactants concentration, water and pressure distributions in the in-flow direction.

The 1+1D model was calibrated and validated on experimental data gathered in the framework of European ID-FAST on a segmented cell hardware. Results highlight the capability of it to correctly reproduce the main transient phenomena occurring in a PEMFC under realistic automotive operating conditions. During Low-Power operation, because of the low water production, the limiting phenomenon is represented by the proton transport across membrane and catalyst layers. Consistently, cathode inlet is the less performing region while the third segment, representing the proper compromise between oxygen availability and local hydration state, is the most performing section of the MEA. In High-Power condition, instead, mass transport becomes the limiting phenomenon and the large fraction of liquid water in channels and porous media significantly hinders reactant diffusion worsening local performance of third and fourth segments. For this reason, with respect to the Low-Power operation, in High-Power cathode inlet becomes the most performing region of the MEA.

Lastly, the effect of air inlet humidification was investigated: an increase in RH from 30% to 50% leads to a slight increase in stack efficiency thanks to a better proton conductivity promoted by the larger λ in CLs and membrane. This effect is particularly evident for segments 1 and 2 whose local performance are significantly enhanced by the less dry operating conditions. On the other hand, the larger water content in the inlet stream and the progressive water accumulation in the along-the-channel direction negatively influence the performance of cathode outlet region, where flooding phenomena in channels and porous media hinder gas diffusion. A decrease in the air inlet humidification from 30% to 15%, instead, determines a worsening in stack efficiency due to the higher ohmic losses originated by the lower water content. This phenomenon particularly affects the cathode inlet region of the cell determining an important performance heterogeneity among the different sections of the MEA.

Therefore, local operating conditions significantly changes in the along-the-channel direction during a real-world automotive driving cycle: this may lead not only to heterogeneities in terms of performance, as described in this paper, but also in terms of degradation which, therefore, must be carefully investigated in future works. In particular, because of the largest water content λ, it is reasonable to think that, for a RH at cathode channel inlet equal or higher than 30%, middle and outlet regions of the cell will be those exposed to the most important ECSA loss. Indeed, in the literature [4,90] it is widely recognized that almost all the main degradation mechanisms are exacerbated in the presence of a large water content. These results highlight the necessity to develop tools able to design proper control strategies aimed at extending lifetime [3] and, being able to correctly predict the effect of operating conditions, the proposed model may be certainly helpful.

CRediT authorship contribution statement

Francesco Verducci: Writing – review & editing, Writing – original draft, Validation, Software, Methodology, Investigation, Formal analysis, Conceptualization. **Amedeo Grimaldi:** Writing – review & editing, Writing – original draft, Validation, Software, Methodology, Investigation, Formal analysis, Conceptualization. **Elena Colombo:** Writing – review & editing, Validation, Investigation, Data curation. **Andrea Casalegno:** Writing – review & editing, Visualization, Project administration, Methodology. **Andrea Baricci:** Writing – review & editing, Methodology, Formal analysis, Conceptualization.

Declaration of competing interest

The authors declare the following financial interests/personal relationships which may be considered as potential competing interests: Andrea Casalegno reports financial support was provided by Ministry of the Environment and Energy Safety.

Acknowledgments

This work received support from the Italian government (Ministero dell'ambiente e della sicurezza energetica - Progetto PERMANENT - BANDO MITE PNRR Missione 2 Investimento 3.5 A - RSH2A_0O0012).

Appendix A. Supplementary data

Supplementary data to this article can be found online at https://doi.org/10.1016/j.renene.2024.121194.

Nomenclature

A	Surface area/m^2
a	Gas activity/-
c	Gas concentration of i-species/mol m^{-3}
d	Thickness of layer i/m
C_{th}	Volumetric thermal capacity/J m^{-3} K^{-1}
c_p	Specific heat capacity/J kg^{-1} K^{-1}
d_h	Hydraulic diameter of gas channel/m
D_i^{mix}	Mixed diffusion coefficient of species i/m^2 s^{-1}
D_i^{eff}	Effective diffusion coefficient of species i/m^2 s^{-1}
D_i^{Kn}	Knudsen diffusivity of species i/m^2 s^{-1}
D_{ij}	Binary diffusion coefficient of gas species i in j/m^2 s^{-1}
$E_{0,i}$	Equilibrium potential of reaction i/V
E_{act}	Activation energy/J mol^{-1}
EW	Equivalent weight of ionomer/g mol^{-1}
F	Faraday's constant/C mol^{-1}
f	Friction factor for pressure losses/-
f_{land}	Geometric correction for GDL/-

f_{th}	Correction factor/-
f_v	Water volume fraction in ionomer/-
h	Height/m
h_m	Mass convective transfer coefficient/m s^{-1}
H^{CC}	Henry constant/mol Pa m^{-3}
$\Delta\widetilde{H}_{ORR}$	Enthalpy change associated to electrochemical reaction ORR/J mol^{-1}
$\Delta\widetilde{H}_{vl}$	Enthalpy change associated to phase change/J mol^{-1}
i	Current density/A m^{-2}
K_{abs}	Absolute permeability/m^2
K_{H_2}	Hydrogen permeability across membrane/mol m^{-1} s^{-1} Pa^{-1}
$K_{r,i}$	Kinetic constant of reduction branch for reaction i/mol m^{-2} s^{-1}
$K_{o,i}$	Kinetic constant of oxidation branch for reaction i/mol m^{-2} s^{-1}
k_{vd}	Interfacial constant of water sorption/m s^{-1}
k_{rel}	Relative permeability/-
k_{vl}	Phase change rate constant in layers/mol m^{-3} s^{-1} Pa^{-1}
$L_{Pt,c/a}$	Catalyst loading at cathode and anode catalyst layer/g m^{-2}
M_i	Molecular weight of species i/g mol^{-1}
$\dot{N}$	Molar flow rate/mol s^{-1}
$\dot{n}$	Mole flux/mol m^{-2} s^{-1}
n_{RIB}	Number of parallel channels/-
p	Pressure/Pa
p_{cap}	Capillary pressure/Pa
R	Transport resistance in governing equation
$\mathscr{R}$	Universal gas constant/J mol^{-1} K^{-1}
$\dot{q}$	Heat flux/W m^{-2}
Re	Reynolds number/-
$r.f.$	Roughness factor/m^2_{Pt} m^{-2}
RH	Relative humidity of gas/-
S	Source term in governing equation
s	Liquid saturation/-
Sc_i	Schmidt number/-
Sh_i	Sherwood number/-
T	Temperature/K
v_i^*	Superficial velocity of phase i/m s^{-1}
v_i	Velocity of phase i/m s^{-1}
V	Volume/m^3
$\overline{V}$	Molar volume/m^3 mol^{-1}
y	Mole fraction/-
w	Width/m
ΔV	Cell voltage/V

Greek letters

α_{liq}	Correction coefficient for the liquid phase velocity/-
$\alpha_{o,i}$	Anodic transfer coefficient for reaction i/
$\alpha_{r,i}$	Cathodic transfer coefficient for reaction i/-
γ_{liq}	Surface tension of water/N m^{-1}
Δ	Difference/
ε	Porosity/-
φ	Potential/V
ς	Correction coefficient in R_{CL}^{eff}/-
$\eta_{d,eff}$	Electro-osmotic drag coefficient/-
λ	Water content in ionomer phase/-
λ_{th}	Threshold ionomer water content for ionic conductivity/-
μ	Gas dynamic viscosity/Pa s
ρ	Density/kg m^{-3}
Γ	Site density of platinum/mol m^{-2}
ω_{PtO}	Energy parameter for Temkin isotherm/J mol^{-1}
ϑ_{PtO}	PtO oxide coverage fraction/-
ϑ_c	Contact angle/-
τ	Tortuosity of porous layer/-
σ	Conductivity/S m^{-1}

Subscripts, superscripts and abbreviations

a	Anode

amb	Ambient
avg	Average
BP	Bipolar plate
c	Cathode side
CH	Channel
CL	Catalyst layer
CV	Control volume
ECSA	Electrochemical active area
eff	Effective property
el	Related to solid phase
eq	Equilibrium conditions
gas	Gas phase
GDL	Gas diffusion layer
HFR	High Frequency Resistance
HOR	Hydrogen Oxidation Reaction
HP	High-Power operation
IN	Inlet
ion	Related to ionomer phase
liq	Liquid water
LP	Low-Power operation
lv	Related to water vapor-liquid phase change
MEM	Membrane
MEA	Membrane-electrode assembly
MPL	Micro-porous layer
ORR	Oxygen Reduction Reaction
OUT	Outlet
PEMFC	Polymer Electrolyte Membrane Fuel Cell
RHE	Reference Hydrogen Electrode
sat	Saturation
SI	Supplementary information
th	Thermal transport
tot	Total
v	Water vapor
vd	Related to water sorption in ionomer

Appendix

A complete list of model variables and parameters is provided in Table A1. The parameter values shown here correspond to the parameters used in the simulation of all the cases reported in this work and the anode and cathode parameters are assumed to be equal unless noted otherwise.

Table A1
– Model parameters

Parameter		Value [Unit]	Reference
A_{MEA}	MEA area	25 cm^2	Mat. Prop.
$C_{th,CHc/a}$	Volumetric heat capacity of gas channels	1.21×10^3/ 1.47×10^3 $J\ m^{-3}\ K^{-1}$	[23]
$C_{th,GDLa/c}$	Volumetric heat capacity of GDLa/c	1.58×10^6 $J\ m^{-3}\ K^{-1}$	[28]
$C_{th,MPLa/c}$	Volumetric heat capacity of MPLa/c	1.98×10^6 $J\ m^{-3}\ K^{-1}$	[28]
$C_{th,CLa/c}$	Volumetric heat capacity of CLa/c	1.56×10^6 $J\ m^{-3}\ K^{-1}$	[28]
$C_{th,MEM}$	Volumetric heat capacity of membrane	1.9×10^6 $J\ m^{-3}\ K^{-1}$	[28]
$d_{GDLa/c}$	GDL thickness	117 μm	Mat. Prop.
$d_{MPLa/c}$	MPL thickness	22 μm	Mat. Prop.
$d_{CLa/c}$	CL thickness	7/10 μm	Mat. Prop.
$d_{h,c/a}$	Hydraulic diameter	9.19×10^{-4} m	Geometry
d_{MEM}	Thickness MEM	15 μm	Mat. Prop.
$E_{act,ORR}$	Activation energy ORR	42 $kJ\ mol^{-1}$	[91]
$E_{0,PtO}$	Equilibrium potential for PtOx formation	0.86 V	[92]
EW	Ionomer equivalent weight	1.1 $kg\ mol^{-1}$	Mat. Prop.
$ECSA_c$	Electrochemical surface area	40 $m^2_{Pt}g_{Pt}$	Mat. Prop.
F	Faraday constant	96485 $C\ mol^{-1}$	Prop.
f_{land}	Geometric corrective factor for mass transport path in GDLa/c	1.4	Fitted
$h_{CH,c/a}$	Channel height	1×10^{-3} m	Geometry
$\Delta\widetilde{H}_{ORR}$	Enthalpy change associated to ORR	-2.42×10^5 $J\ mol^{-1}$	Prop.
$\Delta\widetilde{H}_{vl}$	Enthalpy change associated to liquid-vapor phase change	4.15×10^4 $J\ mol^{-1}$	Prop.
H^{CC}	Henry constant	$3.16 \times 10^{-5}$$mol\ m^{-3}\ Pa^{-1}$	Prop.
$K_{abs,GDLa/c}$	Absolute permeability GDLa/c	3×10^{-12} m^2	Mat. Prop.
$K_{abs,MPLa/c}$	Absolute permeability MPLa/c	1×10^{-12} m^2	Mat. Prop.

(continued on next page)

Table A1 (*continued*)

Parameter		Value [Unit]	Reference
$K_{abs,CLa/c}$	Absolute permeability CLa/c	2×10^{-13} m^2	Mat. Prop.
$K_{o,PtO}$	Forward reaction rate PtO	2×10^{-10} mol m$_{Pt}^{-2}$ s^{-1}	Fitted
$K^*_{r,ORR}$	Kinetic constant ORR	1452 mol m^{-2} s^{-1}	Fitted
$K_{O,HOR}$/ $K_{r,HOR}$	Kinetic constant HOR	0.3/0.3 mol m^{-2} s^{-1}	[41]
k_{vl}	Evaporation/Condensation rate	1 mol Pa^{-1} m^{-3} s^{-1}	[41]
$L_{Pt,a}$, $L_{Pt,c}$	Platinum loading at anode/cathode CL	1/5 g$_{Pt}$m^{-2}	Mat. Prop.
n_{RIB}	Number of parallel channels	3	Geometry
p_{ref}	Reference pressure	101325 Pa	Prop.
R_{el}	Electric resistance of GDLs and BPs	10 mΩ cm^2	Measured
$R^{*Pt}_{O_2,ref}$	Local film-resistance for oxygen transport	1200 s m^{-1}	[52]
$\mathscr{R}$	Universal gas constant	8.314 J mol^{-1} K^{-1}	Prop.
$r_{Kn,MPLa/c}$	Knudsen radius MPLa/c	250 nm	Fitted
$r_{Kn,CLa/c}$	Knudsen radius CLa/c	70 nm	Fitted
T_{ref}	Reference temperature	353.15 k	Prop.
$w_{CH,c/a}$	Channel width	850×10^{-6} m	Geometry
$z_{CHc,a}$	Channel length	0.49 m	Geometry
$\alpha_{r,ORR}$	Symmetry factor ORR	0.5	[49]
$\alpha_{o,PtO}$, $\alpha_{r,PtO}$	Symmetry factor for PtO kinetics	0.25	[49]
$\alpha_{o,HOR}$, $\alpha_{r,HOR}$	Symmetry factor HOR	0.5	[41]
α_{liq}	Liquid velocity in flow channel coefficients	9.5×10^{-4}	Fitted
γ_{liq}	Liquid water surface tension	0.062 N m^{-1}	[30]
γ_s	Exponent for s correction to gas diffusivity	3	Prop.
$\epsilon_{GDLa/c}$	Porosity GDLa/c	0.65	[93]
$\epsilon_{MPLa/c}$	Porosity MPLa/c	0.40	[93]
$\epsilon_{CLa/c}$	Porosity CLa/c	0.35	[93]
$\epsilon_{ion,CLa/c}$	Ionomer volume fraction CLa/c	0.25/0.20	Mat. Prop.
Γ	Site density of Pt	2.1/F mol m^{-2}	Mat. Prop.
K_{liq}	Correction factor for convective mass transport resistance	350 s m^{-1}	Fitted
κ_m	Coefficient of σ_{ion}	50 s m^{-1}	Fitted
λ_{th}	Coefficient of σ_{ion}	1	Fitted
σ_{res}	Coefficient of σ_{ion}	0.3 s m^{-1}	Fitted
$\mu_{gas\ c/a}$	Gas dynamic viscosity at cathode/anode channels	2.1×10^{-5}/1.1×10^{-5} Pa s	[23]
μ_{liq}	Liquid water dynamic viscosity	3.55×10^{-4} Pa s	[30]
ρ_{liq}	Liquid water density	982 kg m^{-3}	[30]
ρ_{ion}	Dry membrane density	1980 kg m^{-3}	Mat. Prop.
$\theta_{GDLa/c}$	Contact angle GDLa/c	110°	Mat. Prop.
$\theta_{MPLa/c}$	Contact angle MPLa/c	130°	Mat. Prop.
$\theta_{CLa/c}$	Contact angle CLa/c	100°	Mat. Prop.
$\tau_{GDLa/c}$	Tortuosity GDLa/c	1.55	[93]
$\tau_{MPLa/c}$	Tortuosity MPLa/c	3	[93]
$\tau_{CLa/c}$	Tortuosity CLa/c	3	[93]

References

[1] E.L. Carlson, K. Pickford, H. Nyga-Łukaszewska, Green hydrogen and an evolving concept of energy security: challenges and comparisons, Renew. Energy 219 (2023) 119410, https://doi.org/10.1016/j.renene.2023.119410.

[2] M. Sadiq, R.J. Alshehhi, R.R. Urs, A.T. Mayyas, Techno-economic analysis of green-H2@Scale production, Renew. Energy 219 (2023) 119362, https://doi.org/10.1016/j.renene.2023.119362.

[3] M. Yue, S. Jemei, N. Zerhouni, R. Gouriveau, Proton exchange membrane fuel cell system prognostics and decision-making: current status and perspectives, Renew. Energy 179 (2021) 2277–2294, https://doi.org/10.1016/j.renene.2021.08.045.

[4] P. Ren, P. Pei, Y. Li, Z. Wu, D. Chen, S. Huang, Degradation mechanisms of proton exchange membrane fuel cell under typical automotive operating conditions, Prog. Energy Combust. Sci. 80 (2020) 100859, https://doi.org/10.1016/j.pecs.2020.100859.

[5] E. Crespi, G. Guandalini, G.N. Cantero, S. Campanari, Dynamic modeling of a PEM fuel cell power plant for flexibility optimization and grid support, Energies 15 (2022) 1–23, https://doi.org/10.3390/en15134801.

[6] S.I. Seleem, H.M. Hasanien, A.A. El-Fergany, Equilibrium optimizer for parameter extraction of a fuel cell dynamic model, Renew. Energy 169 (2021) 117–128, https://doi.org/10.1016/j.renene.2020.12.131.

[7] J. Won, H. Oh, J. Hong, M. Kim, W.Y. Lee, Y.Y. Choi, S. Bin Han, Hybrid diagnosis method for initial faults of air supply systems in proton exchange membrane fuel cells, Renew. Energy 180 (2021) 343–352, https://doi.org/10.1016/j.renene.2021.07.079.

[8] J. Baschuk, X. Li, Modelling of polymer electrolyte membrane fuel cells with variable degrees of water flooding, J. Power Sources 86 (2000) 181–196, https://doi.org/10.1016/S0378-7753(99)00426-7.

[9] T.F. Fuller, J. Newman, Water and thermal management in solid-polymer-electrolyte fuel cells, J. Electrochem. Soc. 140 (1993) 1218–1225, https://doi.org/10.1149/1.2220960.

[10] B.A. McCain, A.G. Stefanopoulou, I.V. Kolmanovsky, A dynamic semi-analytic channel-to-channel model of two-phase water distribution for a unit fuel cell, IEEE Trans. Control Syst. Technol. 17 (2009) 1055–1068, https://doi.org/10.1109/TCST.2008.2005064.

[11] J. Golbert, D.R. Lewin, Model-based control of fuel cells: (1) Regulatory control, J. Power Sources 135 (2004) 135–151, https://doi.org/10.1016/j.jpowsour.2004.04.008.

[12] S. Chevalier, C. Josset, B. Auvity, Analytical solutions and dimensional analysis of pseudo 2D current density distribution model in PEM fuel cells, Renew. Energy 125 (2018) 738–746, https://doi.org/10.1016/j.renene.2018.02.120.

[13] D. Natarajan, T. Van Nguyen, A two-dimensional, two-phase, multicomponent, transient model for the cathode of a proton exchange membrane fuel cell using conventional gas distributors, J. Electrochem. Soc. 148 (2001) A1324, https://doi.org/10.1149/1.1415032.

[14] I.V. Zenyuk, P.K. Das, A.Z. Weber, Understanding impacts of catalyst-layer thickness on fuel-cell performance via mathematical modeling, J. Electrochem. Soc. 163 (2016) F691–F703, https://doi.org/10.1149/2.1161607jes.

[15] A. Goshtasbi, B.L. Pence, T. Ersal, Computationally efficient pseudo-2D non-isothermal modeling of polymer electrolyte membrane fuel cells with two-phase phenomena, J. Electrochem. Soc. 163 (2016) F1412–F1432, https://doi.org/10.1149/2.0871613jes.

[16] E. Colombo, A. Bisello, A. Casalegno, A. Baricci, Mitigating PEMFC degradation during start-up: locally resolved experimental analysis and transient physical modelling, J. Electrochem. Soc. 168 (2021) 054508, https://doi.org/10.1149/1945-7111/abf4eb.

[17] H. Guo, J. Song, F. Ye, M.A. Chong Fang, Dynamic response during mode switching of unitized regenerative fuel cells with orientational flow channels, Renew. Energy 188 (2022) 698–710, https://doi.org/10.1016/j.renene.2022.02.049.
[18] G.S. Kim, P.C. Sui, A.A. Shah, N. Djilali, Reduced-dimensional models for straight-channel proton exchange membrane fuel cells, J. Power Sources 195 (2010) 3240–3249, https://doi.org/10.1016/j.jpowsour.2009.11.110.
[19] L.M. Pant, M.R. Gerhardt, N. Macauley, R. Mukundan, R.L. Borup, A.Z. Weber, Along-the-channel modeling and analysis of PEFCs at low stoichiometry: development of a 1+2D model, Electrochim. Acta 326 (2019) 134963, https://doi.org/10.1016/j.electacta.2019.134963.
[20] H. Wu, P. Berg, X. Li, Steady and unsteady 3D non-isothermal modeling of PEM fuel cells with the effect of non-equilibrium phase transfer, Appl. Energy 87 (2010) 2778–2784, https://doi.org/10.1016/j.apenergy.2009.06.024.
[21] L. Hao, K. Moriyama, W. Gu, C.-Y. Wang, Three dimensional computations and experimental comparisons for a large-scale proton exchange membrane fuel cell, J. Electrochem. Soc. 163 (2016) F744–F751, https://doi.org/10.1149/2.1461607jes.
[22] S.P. Philipps, C. Ziegler, Computationally efficient modeling of the dynamic behavior of a portable PEM fuel cell stack, J. Power Sources 180 (2008) 309–321, https://doi.org/10.1016/j.jpowsour.2008.01.089.
[23] A. Goshtasbi, B.L. Pence, J. Chen, M.A. DeBolt, C. Wang, J.R. Waldecker, S. Hirano, T. Ersal, A mathematical model toward real-time monitoring of automotive PEM fuel cells, J. Electrochem. Soc. 167 (2020) 049002, https://doi.org/10.1149/1945-7111/ab76b5.
[24] Y. Wang, C.-Y. Wang, Two-phase transients of polymer electrolyte fuel cells, J. Electrochem. Soc. 154 (2007) B636, https://doi.org/10.1149/1.2734076.
[25] E. Colombo, A. Baricci, A. Bisello, L. Guetaz, A. Casalegno, PEMFC performance decay during real-world automotive operation: evincing degradation mechanisms and heterogeneity of ageing, J. Power Sources 553 (2023) 232246, https://doi.org/10.1016/j.jpowsour.2022.232246.
[26] F. Wilhelm, E. Colombo, A. Bisello, A. Baricci, A. Casalegno, F. Micoud, S. Escribano, K. Talukdar, P. Gazdzicki, ID-FAST -D4.3 – analysis of coupling between mechanisms and definition of combined ASTs. https://www.id-fast.eu/uploads/media/ID-FAST_D4-3_Analysis_of_coupling_between_mechanisms_and_definition_of_combined_ASTs_OK.pdf, 2021.
[27] B. Müller, T. Mittermeier, A new load cycle and durability test procedure based on vehicle fleet data. https://www.id-fast.eu/uploads/media/ID-FAST_Final_Workshop_2021-12-16_03_Drive_Cycle_public.pdf, 2021.
[28] A. Goshtasbi, P. García-Salaberri, J. Chen, K. Talukdar, D.G. Sanchez, T. Ersal, Through-the-Membrane transient phenomena in PEM fuel cells: a modeling study, J. Electrochem. Soc. 166 (2019) F3154–F3179, https://doi.org/10.1149/2.0181907jes.
[29] M.A. Rahman, F. Mojica, M. Sarker, P.Y.A. Chuang, Development of 1-D multiphysics PEMFC model with dry limiting current experimental validation, Electrochim. Acta 320 (2019) 134601, https://doi.org/10.1016/j.electacta.2019.134601.
[30] H. Wu, X. Li, P. Berg, On the modeling of water transport in polymer electrolyte membrane fuel cells, Electrochim. Acta 54 (2009) 6913–6927, https://doi.org/10.1016/j.electacta.2009.06.070.
[31] D.R. Baker, D.A. Caulk, K.C. Neyerlin, M.W. Murphy, Measurement of oxygen transport resistance in PEM fuel cells by limiting current methods, J. Electrochem. Soc. 156 (2009) B991, https://doi.org/10.1149/1.3152226.
[32] C.K. Mittelsteadt, H. Liu, Conductivity, permeability, and ohmic shorting of ionomeric membranes, in: Handb. Fuel Cells, Wiley, 2010, https://doi.org/10.1002/9780470974001.f500025.
[33] M.C. Leverett, Capillary behavior in porous solids, Trans. AIME 142 (1941) 152–169, https://doi.org/10.2118/941152-G.
[34] J. Sim, M. Kang, H. Oh, E. Lee, J.Y. Jyoung, K. Min, The effect of gas diffusion layer on electrochemical effective reaction area of catalyst layer and water discharge capability, Renew. Energy 197 (2022) 932–942, https://doi.org/10.1016/j.renene.2022.07.096.
[35] D. Ko, S. Doh, H.S. Park, M.H. Kim, Investigation of the effect of operating pressure on the performance of proton exchange membrane fuel cell: in the aspect of water distribution, Renew. Energy 115 (2018) 896–907, https://doi.org/10.1016/j.renene.2017.08.063.
[36] J. Son, Y.B. Kim, Numerical analysis on polymer electrolyte membrane fuel cell performance enhancement with novel selective-patterned gas diffusion layers, Renew. Energy 195 (2022) 455–465, https://doi.org/10.1016/j.renene.2022.06.008.
[37] F. Aldakheel, M.S. Ismail, K.J. Hughes, D.B. Ingham, L. Ma, M. Pourkashanian, D. Cumming, R. Smith, Gas permeability, wettability and morphology of gas diffusion layers before and after performing a realistic ex-situ compression test, Renew. Energy 151 (2020) 1082–1091, https://doi.org/10.1016/j.renene.2019.11.109.
[38] A. Kwong, H. Gunterman, J.T. Gostick, K.T. Clark, A. Kusoglu, A.Z. Weber, Water uptake in PEMFC catalyst layers, ECS Meet. Abstr. MA2011-02 (2011) 830, https://doi.org/10.1149/ma2011-02/16/830, 830.
[39] T. Berning, A. Olesen, S. Kær, On the diffusion coefficient of water in polymer electrolyte membranes, ECS Meet. Abstr. MA2012-02 (2012) 1556, https://doi.org/10.1149/ma2012-02/13/1556, 1556.
[40] V. Liso, S. Simon Araya, A.C. Olesen, M.P. Nielsen, S.K. Kær, Modeling and experimental validation of water mass balance in a PEM fuel cell stack, Int. J. Hydrogen Energy 41 (2016) 3079–3092, https://doi.org/10.1016/j.ijhydene.2015.10.095.
[41] R. Vetter, J.O. Schumacher, Experimental parameter uncertainty in proton exchange membrane fuel cell modeling. Part I: scatter in material parameterization, J. Power Sources 438 (2019) 227018, https://doi.org/10.1016/j.jpowsour.2019.227018.
[42] T.E. Springer, T.A. Zawodzinski, S. Gottesfeld, Polymer electrolyte fuel cell model, J. Electrochem. Soc. 138 (1991) 2334–2342, https://doi.org/10.1149/1.2085971.
[43] A.Z. Weber, J. Newman, Transport in polymer-electrolyte membranes : III. Model validation in a simple fuel-cell model, J. Electrochem. Soc. 151 (2004) A326, https://doi.org/10.1149/1.1639158.
[44] K.C. Neyerlin, W. Gu, J. Jorne, A. Clark, H.A. Gasteiger, Cathode catalyst utilization for the ORR in a PEMFC, J. Electrochem. Soc. 154 (2007) B279, https://doi.org/10.1149/1.2400626.
[45] A. Grimaldi, A. Baricci, S. De Antonellis, C. Oldani, A. Casalegno, Experimental study and modeling of water transport through short-side-chain perfluorosulfonic acid membranes, J. Power Sources 558 (2023) 232556, https://doi.org/10.1016/j.jpowsour.2022.232556.
[46] A. Kusoglu, A.Z. Weber, Water transport and sorption in nafion membrane, in: Polym. Energy Storage Deliv. Polyelectrolytes Batter. Fuel Cells, ACS Publications, 2012, pp. 175–199, https://doi.org/10.1021/bk-2012-1096.ch011.
[47] A.Z. Weber, J. Newman, Transport in polymer-electrolyte membranes : II. Mathematical model, J. Electrochem. Soc. 151 (2004) A311, https://doi.org/10.1149/1.1639157.
[48] W. Yoon, A.Z. Weber, Modeling low-platinum-loading effects in fuel-cell catalyst layers, J. Electrochem. Soc. 158 (2011) B1007, https://doi.org/10.1149/1.3597644.
[49] S. Jomori, N. Nonoyama, T. Yoshida, Analysis and modeling of PEMFC degradation: effect on oxygen transport, J. Power Sources 215 (2012) 18–27, https://doi.org/10.1016/j.jpowsour.2012.04.069.
[50] L. Hao, K. Moriyama, W. Gu, C.-Y. Wang, Modeling and experimental validation of Pt loading and electrode composition effects in PEM fuel cells, J. Electrochem. Soc. 162 (2015) F854–F867, https://doi.org/10.1149/2.0221508jes.
[51] M. Secanell, A. Putz, S. Shukla, P. Wardlaw, M. Bhaiya, L.M. Pant, M. Sabharwal, Mathematical modelling and experimental analysis of thin, low-loading fuel cell electrodes, ECS Meet. Abstr. MA2015-02 (2015) 1307, https://doi.org/10.1149/ma2015-02/37/1307, 1307.
[52] T. Jahnke, A. Baricci, An analytical approximation for the ionomer film model in PEMFC, J. Electrochem. Soc. 169 (2022) 094514, https://doi.org/10.1149/1945-7111/ac94a6.
[53] N. Nonoyama, S. Okazaki, A.Z. Weber, Y. Ikogi, T. Yoshida, Analysis of oxygen-transport diffusion resistance in proton-exchange-membrane fuel cells, J. Electrochem. Soc. 158 (2011) B416, https://doi.org/10.1149/1.3546038.
[54] T. Suzuki, H. Yamada, K. Tsusaka, Y. Morimoto, Modeling of oxygen diffusion resistance in polymer electrolyte fuel cells in the intermediate potential region, J. Electrochem. Soc. 165 (2018) F166–F172, https://doi.org/10.1149/2.0471803jes.
[55] A. Baricci, A. Casalegno, A simple analytical approach to simulate the electrochemical impedance response of flooded agglomerates in polymer fuel cells, Electrochim. Acta 157 (2015) 324–332, https://doi.org/10.1016/j.electacta.2015.01.044.
[56] A. Kongkanand, M.F. Mathias, The priority and challenge of high-power performance of low-platinum proton-exchange membrane fuel cells, J. Phys. Chem. Lett. 7 (2016) 1127–1137, https://doi.org/10.1021/acs.jpclett.6b00216.
[57] T.A. Greszler, D. Caulk, P. Sinha, The impact of platinum loading on oxygen transport resistance, J. Electrochem. Soc. 159 (2012) F831–F840, https://doi.org/10.1149/2.061212jes.
[58] P. Zihrul, I. Hartung, S. Kirsch, G. Huebner, F. Hasché, H.A. Gasteiger, Voltage cycling induced losses in electrochemically active surface area and in H 2/Air-Performance of PEM fuel cells, J. Electrochem. Soc. 163 (2016) F492–F498, https://doi.org/10.1149/2.0561606jes.
[59] T. Jahnke, A. Baricci, C. Rabissi, A. Casalegno, Physical modeling of catalyst degradation in low temperature fuel cells: platinum oxidation, dissolution, particle growth and platinum band formation, J. Electrochem. Soc. 167 (2020) 149001, https://doi.org/10.1149/1945-7111/abbfda.
[60] M. Bhaiya, A. Putz, M. Secanell, Analysis of non-isothermal effects on polymer electrolyte fuel cell electrode assemblies, Electrochim. Acta 147 (2014) 294–309, https://doi.org/10.1016/j.electacta.2014.09.051.
[61] R. Bock, A.D. Shum, X. Xiao, H. Karoliussen, F. Seland, I.V. Zenyuk, O.S. Burheim, Thermal conductivity and compaction of GDL-MPL interfacial composite material, J. Electrochem. Soc. 165 (2018) F514–F525, https://doi.org/10.1149/2.0751807jes.
[62] O. Burheim, P.J.S. Vie, J.G. Pharoah, S. Kjelstrup, Ex situ measurements of through-plane thermal conductivities in a polymer electrolyte fuel cell, J. Power Sources 195 (2010) 249–256, https://doi.org/10.1016/j.jpowsour.2009.06.077.
[63] K. Chintam, D. Richard, A. Baker, R. Borup, J. LaManna, D. Hussey, E. Baltic, D. Jacobson, D. Masten, J. Fairweather, S. Hirano, C. Xu, Water imaging in mirai short-stack provided by USCAR, s, https://doi.org/10.2172/1505950, 2019.
[64] H. Guo, Q. Zhao, F. Ye, An experimental study on gas and liquid two-phase flow in orientated-type flow channels of proton exchange membrane fuel cells by using a side-view method, Renew. Energy 188 (2022) 603–618, https://doi.org/10.1016/j.renene.2022.02.070.
[65] X. Zhang, X. Ma, J. Yang, X. Zhu, S. Tai, S. Shuai, Effect of liquid water in flow channel on proton exchange membrane fuel cell: focusing on flow pattern, Energy Convers. Manag. 258 (2022) 115528, https://doi.org/10.1016/j.enconman.2022.115528.
[66] Y. Yin, Y. Li, Y. Qin, M. Li, G. Liu, J. Zhang, J. Zhao, Ex-situ experimental study on dynamic behaviors and detachment characteristics of liquid water in a transparent channel of PEMFC, Renew. Energy 187 (2022) 1037–1049, https://doi.org/10.1016/j.renene.2022.02.031.

[67] Y. Wang, X. Wang, X. Wang, T. Liu, T. Zhu, S. Liu, Y. Qin, Droplet dynamic characteristics on PEM fuel cell cathode gas diffusion layer with gradient pore size distribution, Renew. Energy 178 (2021) 864–874, https://doi.org/10.1016/j.renene.2021.06.135.
[68] Y. Wang, Porous-media flow fields for polymer electrolyte fuel cells, J. Electrochem. Soc. 156 (2009) B1134, https://doi.org/10.1149/1.3183785.
[69] G. Zhang, L. Wu, Z. Qin, J. Wu, F. Xi, G. Mou, Y. Wang, K. Jiao, A comprehensive three-dimensional model coupling channel multi-phase flow and electrochemical reactions in proton exchange membrane fuel cell, Adv. Appl. Energy. 2 (2021) 100033, https://doi.org/10.1016/j.adapen.2021.100033.
[70] A. Kravos, A. Kregar, Ž. Penga, F. Barbir, T. Katrašnik, Real-time capable transient model of liquid water dynamics in proton exchange membrane Fuel Cells, J. Power Sources 541 (2022), https://doi.org/10.1016/j.jpowsour.2022.231598.
[71] E.C. Kumbur, K.V. Sharp, M.M. Mench, Liquid droplet behavior and instability in a polymer electrolyte fuel cell flow channel, J. Power Sources 161 (2006) 333–345, https://doi.org/10.1016/j.jpowsour.2006.04.093.
[72] A.D. Santamaria, P.K. Das, J.C. MacDonald, A.Z. Weber, Liquid-water interactions with gas-diffusion-layer surfaces, J. Electrochem. Soc. 161 (2014) F1184–F1193, https://doi.org/10.1149/2.0321412jes.
[73] S. Xu, P. Liao, D. Yang, Z. Li, B. Li, P. Ming, X. Zhou, Liquid water transport in gas flow channels of PEMFCs: a review on numerical simulations and visualization experiments, Int. J. Hydrogen Energy 48 (2023) 10118–10143, https://doi.org/10.1016/j.ijhydene.2022.12.140.
[74] D.W. Green, M.Z. Southard, in: Perry's Chemical Engineers' Handbook, ninth ed., McGraw-Hill Education, New York, 2019. https://www.accessengineeringlibrary.com/content/book/9780071834087.
[75] M. Koz, S.G. Kandlikar, Numerical simulation of the interfacial oxygen transport resistance for a PEMFC cathode incorporating water coverage, ECS Meet. Abstr. MA2012-02 (2012) 1334, https://doi.org/10.1149/ma2012-02/13/1334, 1334.
[76] M. Koz, S.G. Kandlikar, Oxygen transport resistance at gas diffusion layer - air channel interface with film flow of water in a proton exchange membrane fuel cell, J. Power Sources 302 (2016) 331–342, https://doi.org/10.1016/j.jpowsour.2015.10.080.
[77] L.M. Pant, S. Stewart, N. Craig, A.Z. Weber, Critical parameter identification of fuel-cell models using sensitivity analysis, J. Electrochem. Soc. 168 (2021) 074501, https://doi.org/10.1149/1945-7111/ac0d68.
[78] A. Goshtasbi, Modeling, Parameter Identification, and Degradation-Conscious Control of Polymer Electrolyte Membrane (PEM) Fuel Cells, University of Michigan, 2019.
[79] V. Kannan, H. Xue, K.A. Raman, J. Chen, A. Fisher, E. Birgersson, Quantifying operating uncertainties of a PEMFC – Monte Carlo-machine learning based approach, Renew. Energy 158 (2020) 343–359, https://doi.org/10.1016/j.renene.2020.05.097.
[80] K.C. Neyerlin, W. Gu, J. Jorne, H.A. Gasteiger, Determination of catalyst unique parameters for the oxygen reduction reaction in a PEMFC, J. Electrochem. Soc. 153 (2006) A1955, https://doi.org/10.1149/1.2266294.
[81] G.A. Futter, P. Gazdzicki, K.A. Friedrich, A. Latz, T. Jahnke, Physical modeling of polymer-electrolyte membrane fuel cells: understanding water management and impedance spectra, J. Power Sources 391 (2018) 148–161, https://doi.org/10.1016/j.jpowsour.2018.04.070.
[82] R.K. Ahluwalia, D.D. Papadias, N.N. Kariuki, J.-K. Peng, X. Wang, Y. Tsai, D. G. Graczyk, D.J. Myers, Potential dependence of Pt and Co dissolution from platinum-cobalt alloy PEFC catalysts using time-resolved measurements, J. Electrochem. Soc. 165 (2018) F3024–F3035, https://doi.org/10.1149/2.0031806jes.
[83] Z. Lu, C. Rath, G. Zhang, S.G. Kandlikar, Water management studies in PEM fuel cells, part IV: effects of channel surface wettability, geometry and orientation on the two-phase flow in parallel gas channels, Int. J. Hydrogen Energy 36 (2011) 9864–9875, https://doi.org/10.1016/j.ijhydene.2011.04.226.
[84] S. Arisetty, Y. Liu, W. Gu, M. Mathias, Modeling platinum oxide growth of PEMFC cathode catalysts, ECS Meet. Abstr. MA2015-02 (2015) 1367, https://doi.org/10.1149/ma2015-02/37/1367, 1367.
[85] M. Zago, A. Baricci, A. Bisello, T. Jahnke, H. Yu, R. Maric, P. Zelenay, A. Casalegno, Experimental analysis of recoverable performance loss induced by platinum oxide formation at the polymer electrolyte membrane fuel cell cathode, J. Power Sources 455 (2020), https://doi.org/10.1016/j.jpowsour.2020.227990.
[86] Y. Wu, J.I.S. Cho, T.P. Neville, Q. Meyer, R. Zeische, P. Boillat, M. Cochet, P. R. Shearing, D.J.L. Brett, Effect of serpentine flow-field design on the water management of polymer electrolyte fuel cells: an in-operando neutron radiography study, J. Power Sources 399 (2018) 254–263, https://doi.org/10.1016/j.jpowsour.2018.07.085.
[87] R. Vetter, J.O. Schumacher, Experimental parameter uncertainty in proton exchange membrane fuel cell modeling. Part II: sensitivity analysis and importance ranking, J. Power Sources 439 (2019) 126529, https://doi.org/10.1016/j.jpowsour.2019.04.057.
[88] G. Zhang, K. Jiao, Multi-phase models for water and thermal management of proton exchange membrane fuel cell: a review, J. Power Sources 391 (2018) 120–133, https://doi.org/10.1016/j.jpowsour.2018.04.071.
[89] N. Kitamura, K. Manabe, Y. Nonobe, M. Kizaki, Development of water content control system for fuel cell hybrid vehicles based on AC impedance, SAE Tech. Pap. (2010), https://doi.org/10.4271/2010-01-1088.
[90] A. Kneer, N. Wagner, A semi-empirical catalyst degradation model based on voltage cycling under automotive operating conditions in PEM fuel cells, J. Electrochem. Soc. 166 (2019) F120–F127, https://doi.org/10.1149/2.0641902jes.
[91] N.M. Marković, B.N. Grgur, P.N. Ross, Temperature-dependent hydrogen electrochemistry on platinum low-index single-crystal surfaces in acid solutions, J. Phys. Chem. B 101 (1997) 5405–5413, https://doi.org/10.1021/jp970930d.
[92] C. Zalitis, A. Kucernak, X. Lin, J. Sharman, Electrochemical measurement of intrinsic oxygen reduction reaction activity at high current densities as a function of particle size for Pt4- xCox/C (x = 0, 1, 3) catalysts, ACS Catal. 10 (2020) 4361–4376, https://doi.org/10.1021/acscatal.9b04750.
[93] A. Grimaldi, Modelling and experimental analysis of pem fuel cells under dynamic real-world conditions focusing on the design of an air humidifier, Politecnico di Milano (2023). https://hdl.handle.net/10589/206693.